

## Statistical reconstruction algorithms for continuous wave electron spin resonance imaging

Imry Kissos<sup>a,b</sup>, Michael Levit<sup>b</sup>, Arie Feuer<sup>a</sup>, Aharon Blank<sup>b,\*</sup>

<sup>a</sup>Electrical Engineering, Technion-Israel Institute of Technology, Haifa 32000, Israel

<sup>b</sup>Schulich Faculty of Chemistry, Technion-Israel Institute of Technology, Haifa 32000, Israel

### ARTICLE INFO

#### Article history:

Received 13 January 2013

Revised 4 April 2013

Available online 17 April 2013

#### Keywords:

ESR

EPR

Microscopy

Imaging

Statistical image reconstruction

PWLS

### ABSTRACT

Electron spin resonance imaging (ESRI) is an important branch of ESR that deals with heterogeneous samples ranging from semiconductor materials to small live animals and even humans. ESRI can produce either spatial images (providing information about the spatially dependent radical concentration) or spectral–spatial images, where an extra dimension is added to describe the absorption spectrum of the sample (which can also be spatially dependent). The mapping of oxygen in biological samples, often referred to as oximetry, is a prime example of an ESRI application. ESRI suffers frequently from a low signal-to-noise ratio (SNR), which results in long acquisition times and poor image quality. A broader use of ESRI is hampered by this slow acquisition, which can also be an obstacle for many biological applications where conditions may change relatively quickly over time. The objective of this work is to develop an image reconstruction scheme for continuous wave (CW) ESRI that would make it possible to reduce the data acquisition time without degrading the reconstruction quality. This is achieved by adapting the so-called “statistical reconstruction” method, recently developed for other medical imaging modalities, to the specific case of CW ESRI. Our new algorithm accounts for unique ESRI aspects such as field modulation, spectral–spatial imaging, and possible limitation on the gradient magnitude (the so-called “limited angle” problem). The reconstruction method shows improved SNR and contrast recovery vs. commonly used back-projection-based methods, for a variety of simulated synthetic samples as well as in actual CW ESRI experiments.

© 2013 Elsevier Inc. All rights reserved.

### 1. Introduction

Electron Spin Resonance Imaging (ESRI) is an important method in the field of magnetic resonance [1], with applications ranging from materials science [2,3] to biology and medicine [4–6]. Unlike the more common method of NMR imaging, ESRI usually requires the addition of exogenous spin probes, such as soluble stable trityl radicals [7] or solid paramagnetic particulates (e.g., lithium octa-n-butoxy 2,3-naphthalocyanine, termed LiNc–BuO [8]), to the sample of interest. Furthermore, due to the short relaxation time of most of these spin species, many ESRI experiments cannot be carried out in the pulsed mode of acquisition and require the use of continuous wave (CW) acquisition. This is done by recording several CW spectra under conditions of static gradients with varying amplitudes and directions to spatially encode the sample signal. Such encoding mechanism results in a set of so-called projections which serve as the basis for the image reconstruction algorithm.

In CW ESRI, it is customary to differentiate between two types of image acquisition modes: (a) Cases where there is only one type

of paramagnetic species in the sample and its ESR spectrum is invariant in space. In such events, the required image includes only information about the spin concentration in space (in 1D, 2D or 3D – purely spatial), while the spectral information is not important (trivial). (b) Cases where there is either more than one paramagnetic species in the sample or a single species but with a space-dependent spectrum (for example, different line-widths due to different O<sub>2</sub> concentrations). In such events, the required image should include both the spin concentration (in 1D, 2D, or 3D) and an additional spectral dimension resulting in an overall 2D, 3D, or 4D spectral–spatial image. The type of image to be acquired determines the type of projections that are to be collected, i.e., their number, angular extent around the object, magnitude of gradients employed and field span. The image is then obtained by making use of some reconstruction algorithm that takes the projections and transform them to an image, as outlined below.

As noted above, for most bio-medical applications, the ESR technique requires the incorporation of a suitable exogenous paramagnetic imaging agent (spin probe) into the system under investigation. To avoid toxicity and/or for other practical reasons, the imaging agents are to be administered in small doses, which often results in noisy projection data. In addition, long data-collection

\* Corresponding author. Fax: +972 4 829 5948.

E-mail address: [ab359@tx.technion.ac.il](mailto:ab359@tx.technion.ac.il) (A. Blank).

times with many acquired projections must be avoided in order to cope with the biological clearance of the imaging agent and/or to acquire several time-resolved images with sufficient time resolution. The purpose of this work is to provide and test a new approach to improved image reconstruction under such limiting conditions as low signal-to-noise ratio (SNR) and a relatively small number of projections. It should be noted that CW ESRI is far less common than other imaging modalities that also make use of projection data, such as magnetic resonance imaging (MRI), positron emission tomography (PET), and X-ray computerized tomography (CT). Although many advanced image reconstruction techniques have been developed for the abovementioned clinical methods, it is not straightforward to implement them in the field of ESR. This is due to the unique nature of CW ESRI that acquires projections that “hide” the spin concentration information within the spectral properties of the sample and also uses static field modulation, which further complicates the spectrum. Furthermore, other modalities do not encounter the limited angle problem (see below), and also CT and PET do not have to cope with a spectral dimension in addition to the three spatial axes.

Here we first provide some theoretical background about the image reconstruction problem in general, and briefly describe the major existing approaches to it. Following that, our algorithm is presented in details and examples are given for the reconstruction of a numerical image phantom based on synthetic projections, and also for the reconstruction of an ESR image based on experimental projection results.

## 2. Theory

### 2.1. The image reconstruction problem in CW ESRI

The images in a CW ESRI acquisition process can be obtained by solving an image reconstruction problem using a specific set of experimentally-acquired projection data [1]. In general, the image reconstruction problem can be defined in the following manner: assuming the existence of an object denoted  $X$  in a  $p$ -dimensional space (in this work, we refer to  $p = 2, 3, \text{ or } 4$ ), then  $\Omega \subset \mathbb{R}^p$  is the support in the object domain imaged by the imaging system. (In this paper, 2D or 3D matrixes and 2D functions are noted with capital letters, while vectors and 1D functions are noted with miniscule letters. Moreover, operators are noted using a superscript  $\sim$ , continuous variables use  $()$  for indexing, and discrete variables use  $[\ ]$ ). The measured projection data  $Y$  is acquired in a two-dimensional space (angle and field position), and the support of the projection domain is  $\mathcal{A} \subset \mathbb{R}^2$ . Our measurement model assumes the following form:

$$y = G \cdot x + v, \quad (1)$$

where  $x \in \mathbb{R}$  denotes the imaged object (when all voxels are arranged in a single vector – see below),  $y \in \mathbb{R}$  denotes the measured projections, also arranged in a single vector (see below),  $G \in \mathbb{R}^2$  is the imaging system matrix, and  $v$  is a noise vector. In the context of ESRI,  $x[j]$  is the spin concentration in the  $j^{\text{th}}$  voxel, where the voxels are indexed starting from  $x[1] = X[1, 1, \dots, 1]$  through  $x[n_1] = X[n_1, 1, \dots, 1]$  and then continuing onto the second index of  $X$  and so on (where  $n_j$  is the size of  $X$   $j^{\text{th}}$  dimension). The measured data is indexed by  $y[i] = Y[\phi, k]$ , where  $\phi$  is the projection angle index and  $k$  is the field position in the spectrum (so  $i = (\phi - 1) \cdot n + k$ , where  $n$  is the number of samples in the recorded spectra). Finally, each component of the  $G$  system matrix, denoted as  $G[i, j]$ , is the detected signal amplitude in the recorded projection spectrum from a unit spin density located at voxel  $x[j]$ , measured in projection position  $y[j]$ . The goal of a reconstruction algorithm is to estimate  $x$  from

$y$  for a given system matrix  $G$  that simulates the physical acquisition process.

Let us now first briefly describe the main types of reconstruction algorithms employed in ESRI to date and then present our own approach, denoted *EsrSr* (Electron spin resonance Statistical reconstruction), and its contribution to the field.

### 2.2. Existing approaches to image reconstruction in CW ESRI

#### 2.2.1. Analytical approaches to image reconstruction and their limitations

For simplicity purposes, we limit our discussion in this section to the case where  $p = 2$ . Thus, the imaged object can be explicitly described by  $x(u_1, u_2) \in \mathbb{R}^2$ . Let  $\tilde{\mathfrak{R}}$  denote the continuous Radon transform operator [1] and  $p_\phi(r)$  the Radon projection at angle  $\phi$ , then  $P = \tilde{\mathfrak{R}}(X)$  and

$$p_\phi(r) = \int X(l \cos(\phi) + r \sin(\phi), l \sin(\phi) - r \cos(\phi)) dl. \quad (2)$$

Let  $\tilde{\mathfrak{R}}^T$  denote the adjoint operator of the continuous Radon transform  $\tilde{\mathfrak{R}}$ , then  $X_1 = \tilde{\mathfrak{R}}^T(P)$ :

$$X_1(u_1, u_2) = \frac{1}{2\pi} \int_{\phi=0}^{2\pi} p_\phi(u_1 \cos(\phi) + u_2 \sin(\phi)) d\phi. \quad (3)$$

In ESRI, the actual projection (recorded spectrum) is affected by a kernel  $s(r)$  that operates on the pure projection data as a convolution:

$$y_\phi(r) = s(r) * p_\phi(r), \quad (4)$$

where  $*$  denotes a 1D convolution and we assume that  $s$  is symmetric. We also denote as  $\tilde{S}_a$  the convolution operator characterized by this symmetric kernel. In cases of pure spatial ESRI,  $s$  is easily obtained by recording a spectrum without any gradients. Thus, we can write the acquired projection data as:

$$Y = \tilde{S}P \quad (5)$$

and the forward system operator  $\tilde{G}$  is given by:

$$\tilde{G} = \tilde{S}\tilde{\mathfrak{R}}. \quad (6)$$

Let us now define the backward system operator  $\tilde{G}^T$ :

$$\tilde{G}^T = \tilde{\mathfrak{R}}^T \tilde{S}^T, \quad (7)$$

where  $\tilde{S}^T$  is the deconvolution operator using  $s(r)$  as a kernel. Those notations can be extended to the discrete case where system operator  $\tilde{G}$  becomes system matrix  $G$  and  $\tilde{S}$  and  $\tilde{\mathfrak{R}}$  are replaced by their discrete representation,  $S$  and  $\mathfrak{R}$ , respectively. The discrete forms will be discussed in more details in Section 3.

Focusing for a moment on pure spatial ESRI, in the special case that  $s(r) = \delta(r)$  (the Dirac delta function),  $y_\phi(r) = p_\phi(r)$ , and assuming continuous data and continuous sampling, the Projection Slice Theorem [9] holds. In such a case, the most common reconstruction method is the analytical method of Filtered Back-Projection (FBP):

$$\hat{x}_{FBP} = \tilde{\mathfrak{R}}^T \cdot (h * y), \quad (8)$$

where  $*$  is a 1D convolution and  $h$  is the ramp filter whose frequency response is given by  $|\omega|$ . The ramp filter has been derived analytically in the continuous space. In the discrete space the FBP is an approximation, and additional filters are also proposed in order to reduce the noise-enhancing effect of the ramp filter. These include the Shepp–Logan [10], Ram–Lak [11] and Hamming [12] filters. Furthermore, for many of those filters it is possible to use a frequency cutoff,  $f_c$ , that defines the highest desired frequency in the projections. A lower  $f_c$  results in a degraded resolution, but also reduces the noise in the image.

In most cases, however, the influence of  $s$  (i.e.,  $s(r) \neq \delta(r)$ ) cannot be ignored, which means that even the approximate *FBP* conditions clearly do not hold any more. In pure spatial ESRI, the common approach in this case is to apply an algorithm of spectral deconvolution to the projections before applying the *FBP* algorithm [1]. A common spectral line-shape would be the derivative of a Lorentzian function. The deconvolution process enhances the high frequencies, often leading to increased noise. As a result, deconvolution, as a pre-processing stage for the projections, has its limits in enhancing the resolution of the final ESRI image, and its efficiency greatly depends on the projections' SNR [13].

The case of spectral–spatial imaging corresponds to an addition of one dimension,  $\zeta$ , to the image, but on the other hand,  $s(r)$  can be considered equal to  $\delta(r)$ . Here, conventional ESRI processing also often employs *FBP* [1]. Another difference between purely spatial and spectral–spatial images is that the latter present the “limited angle” problem. This problem emanates from the finiteness of the available gradient amplitude in the ESRI experiment, limiting the elevation angle from the spatial to the spectral axis [14]. Two examples of algorithms based on *FBP* that were employed to solve this issue are the projection slice algorithm (PSA) [15] and the projection space iteration reconstruction–reprojection (PSIRR) algorithm [16]. Both are mathematically equivalent to a linear interpolation in the angular direction in the image space. If the image in the limited angle area is piecewise linear, then linear interpolation might be reasonable; however, in the case of more realistic images, linear interpolation is not a good estimation. Moreover, PSA applies a non-negativity constraint to improve results, as those are not part of the expected physical solution [17]. However, the original projections obtained in the “derivative form” are always both positive and negative and when used without any pre-processing (in the hope of obtaining a more accurate spectral representation of the sample), would lead to image that can be negative in the spectral dimension, making the implementation of this technique problematic. As we will see below, it can be advantageous to try and reconstruct the image with the spectral information appearing on the spectral axis in the original “derivative form”. This makes it possible to analyze the reconstructed image spectrum on a pixel-wise basis, and then to extract the spatially-dependent spectral features in a much better way.

Another issue of concern in spectral–spatial image acquisition is the need to consider cases where relatively large field modulation amplitudes are employed to enhance SNR, but where good spectral resolution should still be maintained. Here, *FBP* was used in conjunction with line-fitting in the spectral domain to reconstruct back the nonmodulated pure spectral components [18,19]. However, such approach assumes a single type of spectrum in each voxel (as it applies a line-fitting algorithm to a predefined Lorentzian line). Further to this assumption that does not always hold, at low SNR levels this parametric method has problems estimating the central position of the spectrum and its full width at half maximum (FWHM), which can lead to unstable results.

It can be summarized that, due to the collective effect of the *FBP* approximations and the deconvolution procedure (for purely spatial ESRI), this reconstruction algorithm is far from being optimal. The problems are usually more pronounced when the acquisition suffers from a low SNR and/or for a limited number of projections. In such cases, the image reconstructed by *FBP* includes known streaking artifacts that are more intense in image periphery and appear as lines emanating from regions of high spin density [20]. Other types of artifacts, such as Gibbs phenomena (visible as ringing and overshoots), are typically caused by inadequate radial sampling rates. Artifacts of this type are more intense in regions where the image changes rapidly [1].

### 2.2.2. *FBP*-based numerical methods for improved image reconstruction

In order to overcome the *FBP* artifacts mentioned above, some previous works have employed pre-processing of the projections before running the *FBP* and/or added a post-processing procedure on the resulting image. An iterative method for pre-processing using a nonlinear fit to the projection data has been shown to produce ripple-free images [21]. When introducing this idea into a multiplicative simultaneous iterative image reconstruction technique (MSIRT), deconvolution is executed as preprocessing and only the Hamming smoothing function is introduced into the reconstruction. This and other similar preprocessing methods [13] are still suboptimal since object constraints such as nonnegativity and piecewise smoothness are not naturally expressed in the projection domain  $\Lambda$ . Also, no specific consideration of noise distribution is taken into account in the reconstruction process. Other works add a post-process to the final image in order to cancel the streaking and Gibbs artifacts using some prior knowledge [22]. Such space-invariant postsmoothing the disadvantage of not incorporating nonstationary measurement statistics since smoothing is not adaptive to the SNR of the processed region. Furthermore, the algorithm requires prior knowledge about the image type, which can constrain this type of processing.

It can be summarized that methods based on *FBP* often suffer from the fact that it is an approximation of an idealized mathematical model of continuum measurements, that they do not consider modulation as an integral part of the reconstruction, and that they do not account for specific noise statistics. However, thanks to the linear nature of *FBP*, it is relatively easy to implement such methods and to analyze their properties.

### 2.2.3. Iterative reconstruction algorithms

**2.2.3.1. Algebraic methods.** Other types of approaches try to overcome some of the abovementioned limitations of the *FBP* algorithms using algebraic iterative methods known as ART and MART [23,24]. These models assume noiseless projections  $y = Gx$  and aim at finding the solution of  $\hat{x}_{\text{Algebraic}} = G^{-1}y$  algebraically. This approach is far from optimal as the system is underdetermined and is not robust, leading to a behavior where small changes in  $y$  may cause a large change in the reconstructed image  $\hat{x}_{\text{Algebraic}}$ .

**2.2.3.2. Statistical methods.** A more generalized view that allows characterizing different types of approaches for iterative image reconstruction algorithms is based on the notion of “statistical methods for image reconstruction” [25]. All statistical methods can be characterized through a general objective function to be minimized, which is:

$$\Phi(X) = \underbrace{\Psi(Y, X)}_{\text{Data Fit}} + \beta \cdot \underbrace{R(X)}_{\text{Penalty}}, \quad (9)$$

where  $\Psi$  fits the object  $X$  to the measured data  $Y$ ,  $R(X)$  is a penalty function that encourages realistic estimates of the object  $X$ , e.g., smoothness, and  $\beta$  is a positive real value that defines the intensity of the penalty function. In general, when employing statistical methods, the choice of the objective function takes into consideration also the noise in the measurements and its distribution in view of the physical measurement process. This leads to better reconstructed image results under conditions of low SNR. Another advantage of statistical reconstruction is that the projections do not need to be equally spaced as in *FBP*. In general, it is known that for a limited number of projections statistical methods for image reconstruction yield higher-quality images than *FBP* reconstruction, but at a price of increased computation [25].

Statistical reconstruction methods relying solely on data fit functional criteria ( $\beta = 0$ ) often produce images that become

unacceptably noisy as the iterations proceed. Methods for avoiding this problem include: (i) stopping the iteration before the images become too noisy (long before convergence) [26], (ii) iterating until convergence and then post-smoothing the image [27]; (iii) using smooth basis functions [27]; and (iv) adding a roughness penalty to encourage image smoothness, meaning  $\beta > 0$  [28]. The penalizing approach to noise reduction has two important advantages over alternatives such as stopping rules and postprocessing. First, the penalty function improves the conditioning of the problem, so certain iterative algorithms converge quickly. Second, it is possible to choose penalty functions that control the desired properties of the reconstructed images, such as preserving edges [28] or incorporating anatomical side information [29,30]. In contrast, the level and type of smoothness that one obtains through stopping rules is much less defined and is limited by the characteristics of the iterative algorithm. It is known that the global smoothing parameter  $\beta$  controls an overall tradeoff between resolution and noise: larger  $\beta$ s lead to coarser resolution but less noise, and vice versa [31].

An example of the use of statistical methods in the field of ESRI is the maximum entropy method, in which the penalty function is defined as

$$\begin{aligned} \text{Entropy}[X] &= -\sum_{i=1}^n pb(x[i]) \cdot \log(pb(x[i])) \text{ or } \text{Entropy}[X] \\ &= -\sum_{i=1}^n \log pb(x[i]). \end{aligned} \quad (10)$$

In the statistical framework,  $X$  is considered to be a random variable and  $pb$  denotes its probability density function. The second definition of the entropy is termed the “Burg entropy”. It is said that the entropy penalty function does not introduce correlations into the data beyond those required by the data itself [32]. The solution that maximizes the entropy is the one which has the lowest information content.

The maximum entropy method was used in the case of spatial–spatial imaging; where Burg entropy was used, and the method was termed LSEnt [33]. It has been shown that the LSEnt method yields results that are better than *FBP* and are comparable to the MART algorithm. In the case of spectral–spatial imaging, a similar approach called MEM [34] has been used. It should be noted that entropy is maximal for an  $X$  that has a uniform distribution, which means that the optimization algorithm “pushes” to such a result which is far from most of the realistic results found in ESRI. Moreover, entropy is a nonlinear operator that poses a problem for the analytical evaluation of its performance. Another problematic issue with these maximum entropy methods is that they do not take into account the field modulation effect as an integral part of the reconstruction process and only account for it during the pre- or post-processing stages. Finally, entropy is a global statistical criterion, as it depends only on  $pb$ , and this means that important local features in the image may be lost or distorted.

### 2.3. Our work – the *EsrSr* algorithm

In this work we make use of the general framework of statistical image reconstruction methods and apply it to the field of ESRI for the first time. The new *EsrSr* algorithm introduced here allows us to achieve improved reconstruction performances compared to *FBP*, under limiting conditions of low SNR levels and a small number of projections. The statistical method chosen in this work takes into account a noise model that is characteristic of ESRI data acquisition. Furthermore, in the *EsrSr* approach, field modulation is integral to the reconstruction algorithm, thus leading to a more accurate physical model, and is not treated during some pre- or

post-processing stages. Other important issues in this work are that, in the case of spatial–spatial imaging, it solves an optimization problem with an algorithm that automatically constrains the original image non-negativity (representing the paramagnetic species concentration); in the case of spectral–spatial images (1D or 2D spatial), the algorithm, which in general can consider any type of “missing data” [35], is used to solve the “limited angle” problem. Further to that, when considering spectral–spatial images we can look at cases that employ modulation amplitudes that are 1–4 times the intrinsic line-width of the spin probe in order to increase the SNR, with the image reconstruction algorithm capable of recreating the original line-width. In that respect, the *EsrSr* approach avoids the assumptions and pitfalls of the line-fitting method described above and thus may be useful, for example, for *in vivo* oxygen experiments providing improved accuracy of line-width measurements under conditions of inadequate SNR. Thus, both the “limited angle” and the issue of a large field modulation can be accounted for at the same time during spectral–spatial (2D) image reconstruction. It should be noted that, to our knowledge, no iterative algorithm has been applied to spectral–spatial CW ESR imaging with spatial dimensions larger than 1.

### 3. Forward problem – the ESRI signal, its projections, and the system’s noise

We start our description of the reconstruction method by first looking at the forward problem, leading from a sample with a specific set of spatially-dependent spin concentration and ESR spectra, to a set of projections. First and foremost, the formulation of the forward problem is needed as part of the iterative process, where the matrices  $G$  and  $G^T$  are employed (see also below). Furthermore, the forward process is also needed to generate the synthetic projections from predefined test samples that are used for algorithm testing.

#### 3.1. The ESRI signal as a function of field modulation

The effects of magnetic field modulation on the resonance line-shape were studied already in the early 1960s [36]. Wahlquist pointed out that when the modulation amplitude equals 2 times the intrinsic half width at half maximum (HWHM) of the line, the ESR signal reaches its maximum. While such relatively large modulation amplitudes lead to an improved SNR, they also degrade the spectral resolution. However, since the mechanism of spectral broadening can be well characterized, one can in principle reconstruct back the native spectral resolution from the over-modulated spectrum. Hyde et al. [37] proposed a filtering algorithm (pseudo-modulation) to simulate the effect of sinusoidal magnetic field modulation and recover the intrinsic spectra of the sample. The pseudo-modulation technique was successfully applied for spectral resolution enhancement [38] and was recently justified by Nielsen and co-workers by solving the Bloch equation [39]. Robinson et al. [40,41] published a universal model to simulate the experimental ESR spectra in liquids by incorporating both modulation amplitude and frequency. They demonstrated that with a precisely-known modulation amplitude, the intrinsic line-width could be accurately extracted through curve fitting of the over-modulated (up to 20 times its intrinsic line-width) spectra. Based on Robinson’s model, Mailer et al. [19] recently reported a remarkable precision improvement in the line-width measurement of the deoxygenated OX031 spin probe using ESR spectral–spatial imaging.

Here we employ Robinson’s model [40,41] to calculate the effects of field modulation and incorporate them in the forward system projector operator, according to Eq. (6), where  $\bar{S}$  includes the

effect of the field modulation. First, we consider the CW ESR spectrum of a point sample with unit amplitude located in the origin, having a Lorentzian ESR line-shape with an intrinsic FWHM of  $\tau$ . The spectrum for such a sample is given by the expression:

$$\text{Signal}(r) = -\frac{1}{\pi \left( (B_0 - r)^2 + i \left( \frac{\tau}{2} \right)^2 \right)}, \quad (11)$$

where  $i = \sqrt{-1}$ . Using Eq. (12) one can define the absorption spectrum as  $s_{Lo}(r) = \text{Im}(\text{signal}(r))$ .

We now add the effect of magnetic field modulation with amplitude  $B_m$  and frequency  $f_m$ . According to Robinson's model [40,41] the in-phase, first-harmonic ESR signal is then expressed as:

$$\text{signal}_1(r) = B_m \cdot \left[ \frac{1}{\tilde{g}_0 \tilde{g}_1^-} + \frac{1}{\tilde{g}_0 \tilde{g}_1^+} \right], \quad (12)$$

where  $\tilde{g}_1^\pm = \frac{1}{2} a_\mp^\pm \left[ 1 + \sqrt{1 - \left( \frac{B_m}{2a_\mp^\pm} \right)^2} \right]$ ,  $\tilde{g}_0 = a_0 - \left( \frac{B_m}{4} \right)^2 \left[ \frac{1}{\tilde{g}_1^-} + \frac{1}{\tilde{g}_1^+} \right]$  and  $a_0 = (B_0 - r)^2 + i \left( \frac{\tau}{2} \right)^2$ ,  $a_\mp^\pm = a_0 \pm \frac{f_m}{\gamma}$ , where  $\gamma$  is the electron gyromagnetic ratio. We chose  $f_m = 100$  kHz for all our results. Following this, it is possible to define

$$s_{Ro}(r) = \text{Im}(\text{signal}_1(r)) \quad (13)$$

as the signal that simulates the effect of modulation.

### 3.2. The forward system operator $\tilde{G}$ generating the projections

We can now continue with the formulation of the forward problem, described by the forward system matrix  $G$  that is the discrete representation of the forward system operator  $\tilde{G}$  in Eq. (6).

#### 3.2.1. Discrete Radon transform $\mathfrak{R}$

The continuous Radon transform  $\tilde{\mathfrak{R}}$  in Eq. (2) has a discrete counterpart,  $\mathfrak{R}$ . Let's denote  $\bullet$  as the rounding function to the closest integer. Then  $p_\Phi[r] = \mathfrak{R}[X]$ :

$$p_\Phi[r] = \sum_{l=l_0}^{l_n} X[l \cos(\Phi) + r \sin(\Phi)], [l \sin(\Phi) - r \cos(\Phi)] \quad (14)$$

The discrete Radon transform for this case is implemented using the 2D parallel-beam system model based on finely-tabulated footprints [42]. Explicitly,  $\mathfrak{R}$  is the discrete Radon transform that sums up all pixels in its projection line  $(\Phi, r)$  into  $p_\Phi(r)$ .

#### 3.2.2. Spatial-spatial images

As noted above, the system operator also includes the effect of modulation denoted by  $S$  in Eq. (6), calculated using Robinson's model in Eq. (14). In practice,  $S$  is implemented via a convolution using  $s_{Ro}[r]$  on the projections:

$$y[n] = S_{Ro}\{p\}[n] = \{s_{Ro} * p\}[n] = \sum_{m=0}^{\text{Length}-1} s_{Ro}[m] \cdot p[n - m]. \quad (15)$$

The incorporation of the convolution into the system operator simulates the physical effects of the measurements. It may be argued that the real physical effect is, first, modulation (expressed mathematically via convolution), and then projection (the mathematical Radon transform). In fact, the Radon convolution theorem states that these operators commute [43], namely,  $\tilde{\mathfrak{R}}(X * s_{Ro}) = \tilde{\mathfrak{R}}(X) * s_{Ro} = P * s_{Ro} = Y$ .

#### 3.2.3. Spectral-spatial images

In the case of spectral and 2D spatial imaging, the discrete Radon transform is implemented with a three-dimensional point-based system model [44]. Explicitly,  $\mathfrak{R}$  becomes the discrete Radon transform that sums up all voxels on a certain plane whose normal

direction is defined by the angles  $\Phi, \eta$  and its position by  $r$  to get  $p_{\Phi, \eta}[r]$ .

When the materials in the image have different line-widths, it is impossible to know *a priori* what would be the forward matrix  $G$  since the effect of modulation would depend on the local line-width of each pixel. Nevertheless, the iterative algorithm needs a well-defined forward matrix to be properly implemented. Therefore, for purposes of forward problem calculation, this work assumes that the FWHM of the materials in the image is the same. Thus, the effect of modulation can be approximated by using a constant kernel with a width that is the average width of the materials' FWHM. In practice, this is carried out by first finding some average FWHM value from the zero gradient projection and then building the function  $s_{Ro}^{\text{average}}[r]$  according to Robinson's model, which is defined as:

$$s_{Ro}^{\text{average}}[r] \equiv s_{Ro}[r]_{\tau=\text{Average FWHM}}. \quad (16)$$

Now, for the forward problem we can first apply  $S$  as a convolution of  $s_{Ro}^{\text{average}}[r]$  on the spectral dimension of  $X$  in the image domain  $\Omega$ , and then apply the Radon transform. The spectral-2D spatial system matrix is then:

$$G = \mathfrak{R}S. \quad (17)$$

And from this matrix it is easy to calculate the transpose  $G^T$  that is needed for the iterative algorithm.

In case we need to create synthetic projections out of a simulated phantom, we use  $G_{\text{first}}$  that incorporates the knowledge of the exact line-shape in each spatial position. In this case,  $G_{\text{first}} = \mathfrak{R}$ , as each spatial position in the phantom has the exact line-shape according to its  $\tau$  value.

### 3.3. Noise model of the ESRI acquisition system

An important feature of our model, especially when trying to apply it under the constraint of a low SNR, is the noise behavior. First, we assume that the sample image  $X$  is stationary in time and does not contain noise. The only source of noise is assumed to be white Gaussian noise in the projection space obtained during the acquisition process. In that respect, we assume that the noise is additive and signal-independent, similar to the approach of Ref. [45]. Such kind of noise distribution is normally justified in ESR since it originates from the electronic Johnson noise of the instrument at the modulation frequency. It should be noted that, in some cases, empirical results showed that the noise is not white, especially for large values of the modulation amplitude and long time constant of the lock-in amplifier [45]. In case the noise is not white, effective prewhitening [46] of the measured signal can be carried out as a standard procedure that can be applied in most cases. Moreover, the statistical framework is general and can be adapted to many types of noise distribution, such as: Poisson [47], Shifted Poisson [48], Poisson + Gaussian (photon variability and electronic readout noise) [49], and compound Poisson [50]. Also, it is possible to empirically estimate the noise distribution in a specific system and apply it to the algorithm, if necessary. In calculating the projections for phantom synthetic samples, the noise is added to each projection according to the SNR, where  $\text{SNR} = \frac{\max(y_\Phi^{\text{phantom}})}{\text{s.d.}(\text{noise})}$ , and s.d. represents the standard deviation of noise.

## 4. Backward problem – the statistical reconstruction

The backward problem can be defined as reconstructing the image  $X$  given the projections  $Y$  and the system matrix  $G$ . As mentioned above, in this work we employ the statistical reconstruction method to solve this problem (see Section 4.2),

but for this solution we need the backward system matrix and the discrete adjoint Radon transform.

#### 4.1. The backward system matrix $G^T$

The backward operator  $\tilde{G}^T$  in Eq. (7) has a discrete counterpart,  $G^T = \mathfrak{R}^T S^T$ . In the case of spatial–spatial imaging,  $S^T$  is implemented by deconvolution using  $s_{Ro}[r]$  in the projection space  $\Lambda$ . In the case of spectral-2D spatial images we use  $G^T = S^T \mathfrak{R}^T$ , the adjoint operator of the forward problem in Eq. (18), where  $S^T$  applies a deconvolution using  $s_{Ro}^{average}[r]$  as described in Eq. (17) on the spectral dimension in the image space  $\Omega$ .

#### 4.2. Discrete adjoint Radon transform $\mathfrak{R}^T$

The adjoint Radon transform  $\tilde{\mathfrak{R}}^T$  (see Eq. (3)) has its discrete counterpart  $\mathfrak{R}^T$  defined by  $X_1 = \mathfrak{R}^T[p_\phi]$ :

$$X_1[u_1, u_2] = \frac{1}{2\pi} \sum_{\phi=0}^{2\pi} p_\phi [u_1 \cos(\phi) + u_2 \sin(\phi)]. \quad (18)$$

In the spatial–spatial reconstruction,  $\mathfrak{R}^T$  puts the projection value at position  $\phi$ ,  $r$  into all the pixels along its projection line. In the case of spatial-2D spectral reconstruction,  $\mathfrak{R}^T$  places the projection value at position  $\phi$ ,  $\eta$ ,  $r$  into all the voxels along its projection plane.

#### 4.3. Objective function of the statistical reconstruction

Most statistical methods for image reconstruction require minimizing an objective function related to the measurement statistics. Namely, the process of finding the most suitable  $X$  based on the projection data  $Y$  and our noise model can be transformed into a problem of finding the minimum of a suitable objective function. For realistic image sizes, direct minimization methods are computationally intractable, so iterative methods are required. Objective functions should be quadratic, or at least convex and locally quadratic, in order to be suitable for fast iterative algorithms such as preconditioned conjugate gradients (PCG) and separable paraboloidal surrogates (SPS), which are appealing for reasons of convergence rate, simplicity, and potential for parallelization [51].

In this work we use the maximum likelihood estimator,  $\hat{x}_{ML} = \text{ArgMax}_x \text{Pb}(x|y)$ , where  $\text{Pb}(x|y)$  is the conditional probability of the image  $x$  given the projections  $y$ . For zero-mean Gaussian noise, the maximum likelihood estimator is equivalent to the least-square estimator,  $\hat{x}_{LS} = \text{ArgMin}_x \|y - Gx\|^2$  [52]. As noted above, in this work we employ a statistical criterion that the distribution of the noise is white and Gaussian, leading to the following penalized weighted least-squares (PWLS) objective function [53]:

$$\Phi(x) = \underbrace{\|W \cdot (Gx - y)\|_2^2}_{\text{Data Fit}} + \beta \cdot \underbrace{R(x)}_{\text{Penalty}}, \quad (19)$$

where  $R(x)$  is a penalty function that encourages smooth or piecewise-smooth estimates, and  $\beta$  is a parameter that controls the tradeoff between spatial resolution and noise [31]. Our goal is to compute an estimate  $\hat{x}_{EsrSr}$  of  $x$  from  $y$  by finding the minimizer of the objective function  $\Phi(x)$ . In addition,  $R(x)$  influences the robustness of the solution, so a minor change in  $Y$  will not greatly affect the resulting  $\hat{x}_{EsrSr}$ . The matrix  $W$  is a positive and diagonal that applies a different weight for every measurement: a larger weight  $w_i$  affects the objective function more strongly and therefore larger importance is given to the corresponding measurement. In our case we use  $W = \frac{1}{\sigma} \cdot I$ , where  $\sigma$  is the standard deviation of the noise. In the case of spectral-2D spatial imaging, the “limited angle” problem is naturally solved using the  $W$  matrix. That is, the corresponding  $W$

entry for the missing angles is simply set to zero. Assuming that the Fourier transform of  $s(r)$  is nonzero at  $\omega_r = 0$  and  $R$  is the differentiator operator  $R: R(X) = (\frac{\partial X}{\partial u_1})^2 + (\frac{\partial X}{\partial u_2})^2$ , one can write the minimizer of Eq. (20) as [31]:

$$\hat{X}_{EsrSr} = [G^T W G + \beta R]^{-1} G^T W \cdot Y. \quad (20)$$

#### 4.4. Regularization

It is worthwhile to discuss the reasons for using regularization and the nature of regularization employed in this work. The solution for the nonregularized problem ( $\beta = 0$ ) with equal weights ( $W = I$ ) is achieved by the pseudoinverse of  $G$ :  $\hat{X}_{LS} = [G^T G]^{-1} G^T \cdot Y$ . However, the nonregularized problem is poorly conditioned or even underdetermined, so some regularization is required to ensure a stable solution. Gradient-based iterative methods generally converge only to local minima for nonconvex regularizing functions, so we focus here on convex penalty functions [54].

For ESRI we have two types of regularization: As noted above, in the case of spatial–spatial imaging we use  $R(X) = (\frac{\partial X}{\partial u_1})^2 + (\frac{\partial X}{\partial u_2})^2$  and we assign equal weights to both axes, as the final image is isotropic. This regularization leads to a locally-better resolution/noise tradeoff than *FBP*. In the case of spectral–spatial imaging we use a weighted version of the regularization function  $R(X) = (\frac{\partial X}{\partial u_1})^2 + (\frac{\partial X}{\partial u_2})^2 + w_\zeta (\frac{\partial X}{\partial \zeta})^2$ , where  $\zeta$  is the spectral dimension and  $w_\zeta > 0$  is the weight assigned to the spectral dimension's penalty. The reason for using  $w_\zeta$  that is not necessarily equal to 1 is because, in the spectral–spatial image, the typical derivative along the spectral dimension may be significantly different from that of the spatial derivative and this has to be accounted for. The value of  $w_\zeta$  can be chosen using prior knowledge based on the *FBP* results or from analytical analysis. The *FBP* results can be used to calculate the average ratio between the measured spatial and spectral derivatives, and this will be the  $w_\zeta$  value for the statistical reconstruction. This adaptation makes better use of our prior knowledge in spatial–spectral imaging.

### 5. Methods

The *EsrSr* algorithm was coded using Matlab and the reconstruction toolbox of Prof. Fessler [42].

#### 5.1. Computational platform

The forward/backward system matrix and optimization algorithm are the most intensive computationally and they are implemented in a fully parallelized fashion. We used 8 computational threads on an Intel© platform with 6 quad-core processing units, totaling 24 cores at 3.2 gigacycles/s and with 24 gigabytes of RAM memory. On this platform, one iteration of the iterative algorithm for the spatial–spatial simulation case lasts 0.15 s for a reconstructed image of  $128^2$  pixels and projection size  $180 \times 140$  [angular samples  $\times$  radial samples]. For the spectral-2D spatial simulation, one iteration lasts 13 s for a reconstructed image of  $128^3$  voxels and projection size  $512 \times 140$  [angular samples  $\times$  radial samples].

#### 5.2. Optimization algorithm and initial image conditions

In the case of spatial–spatial images, the *EsrSr* algorithm uses the SPS [55] optimization algorithm in order to constrain image nonnegativity with fast convergence. The PCG [51] optimization algorithm is used for obtaining fast unconstrained optimization (faster than the SPS that is constrained) in cases where spectral

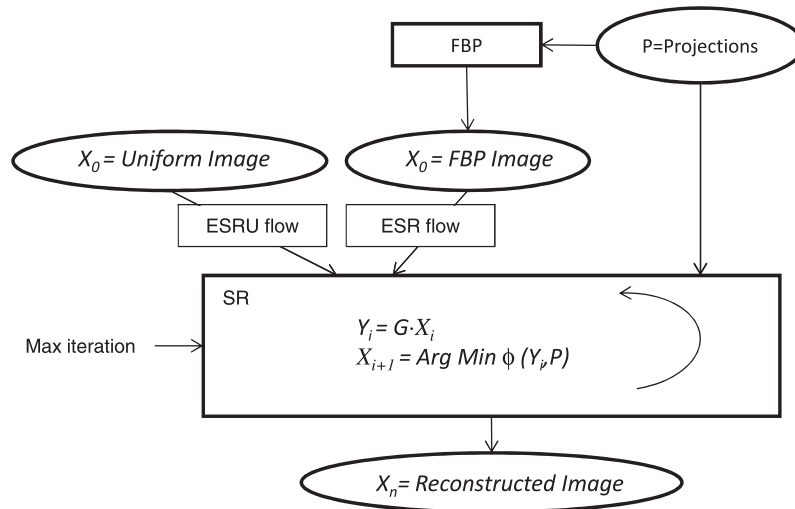


**Fig. 1.** Flowchart schematically showing the different processing approaches using EsrSr and EsrSrU. The raw projections  $P$  are used to create the FBP image and inside the Statistical Reconstruction algorithm. The EsrSrU starts from a uniform image  $X_0$  while the EsrSr starts from the FBP image. The stopping criterion of the algorithm is a specified maximum number of iterations  $n$ , and  $X_n$  is the final reconstructed image.

reconstruction is required in one of the image axes. As for initial image conditions, in some of the calculations we used a uniform image denoted here as *EsrSrU*. Alternatively, in other cases we used the *FBP* reconstructed image result as the initial image for the *EsrSr* to see the added contribution of our method to the image quality. A flow chart describing the reconstruction procedure is presented in Fig. 1.

### 5.3. Simulated and experimental input data

#### 5.3.1. 2D spatial-spatial data

The forward problem algorithm described in Section 3.2.2 was used to simulate the projection results for a Shepp–Logan phantom [56]. The simulated projections were obtained for uniform angular sampling. The projection size was  $180 \times 140$  [angular samples  $\times$  radial samples], while the final reconstructed image size was  $128 \times 128$  pixels. The experimental results of a test sample with 2 crystals of lithium phthalocyanine (LiPc) and one crystal of LiNc–BuO free radicals, described in [57] (see also Section 6.2 below), were collected with uniform sampling of  $256 \times 256$  [angular samples  $\times$  radial samples]. In order to evaluate our algorithm we subsampled the raw data into  $64 \times 256$  [phi Samples  $\times$  radial samples]. The final reconstructed image size was  $128 \times 128$  pixels, corresponding to a physical image size of  $\sim 500 \times 500$  ( $\mu\text{m}^2$ ).

#### 5.3.2. Spectral-2D spatial data

The simulated results were obtained using the forward problem algorithm described in Section 3.2.3. The sample model is a Shepp–Logan phantom to which we added a spectral dimension (a symmetric Lorentzian line, with position-dependent linewidth – see Section 6.1.2). The simulated projections size was  $512 \times 140$  [angular samples  $\times$  radial samples], with maximum theta angle of  $86.3^\circ$ . For each spectral angle [ $86.3^\circ$  to  $-86.3^\circ$  using 16 samples] we sampled the spatial angle [ $0-360^\circ$  using 32 samples]. The reconstructed image size was  $128^3$  pixels. The experiments in spectral-2D spatial imaging were performed with a sample that is described in details in Section 6.2. The projection size was  $4096 \times 256$  [angular samples  $\times$  radial samples] with maximum theta angle limited to  $86.3^\circ$ . In order to evaluate our algorithm we subsampled the raw data into  $1024 \times 256$  [angular samples  $\times$  radial samples]. For each spectral angle [ $86.3^\circ$  to  $-86.3^\circ$  using 16 samples] we sampled the spatial angle [ $0-360^\circ$  using

$256/64$  samples]. The reconstructed image size was  $128^3$  pixels which correspond to and image size of  $500 \times 500 \times 2$  [ $\mu\text{m} \times \mu\text{m} \times G$ ].

#### 5.3.3. Image quality assessments

In order to quantitatively analyze the quality of the reconstructed image, we define a normalization parameter  $c = \frac{\sum_{i=1}^n \text{Phantom}(x[i])}{\sum_{i=1}^n \text{Image}(x[i])}$ , where  $n$  is the total number of pixels or voxels in the final image. Thus, the Mean Square Error is defined as:

$$\text{MSE} = \frac{1}{\sqrt{\sum_{i=1}^n \text{Phantom}(x_i)^2}} \times \sqrt{\sum_{i=1}^n (\text{Phantom}(x[i]) - c \cdot \text{Image}(x[i]))^2}. \quad (21)$$

This kind of measurement is quite standard in the image-processing community.

The MSE takes account of the noise increase as well as the resolution decrease in the reconstruction image. Another type of image quality measurement is the Relative Squared Error (RSE), which measures how close is the spin distribution within the reconstructed image to the true spin distribution [58]:

$$\text{RSE} = \sqrt{\frac{\sum_{i=1}^n (\text{Phantom}(x_i) - c \cdot \text{Image}(x_i))^2}{\sum_{i=1}^n \text{Phantom}(x_i)^2}}. \quad (22)$$

This kind of measurement takes into account the relative error. Since RSE is defined up to a constant factor, in our case we chose to multiply Eq. (23) by 1/100 so that the RSE and the MSE can be presented on the same graph in a similar scale. The RSE gives lower weight to high intensity pixels; this is a dominant phenomenon, especially at the edges. For this reason, the RSE is quite insensitive to resolution loss.

In the case of spectral-spatial images, a one-dimensional cut along the spectral axis of the reconstructed image can be compared to the original one on the phantom by means of the Contrast Recovery (CR) factor given by:

$$\text{CR} = \frac{\max(\text{profile}(\text{Image}))}{\max(\text{profile}(\text{Phantom}))} \cdot 100\%. \quad (23)$$

The contrast recovery of the main lobe, denoted by CRM, is defined on the main lobe section of the profile and should be maximal for a good reconstruction algorithm. On the other hand, the contrast recovery of the side lobes, denoted by CRS, is defined on the rest of the profile and should be minimal. That is, in a single line spectrum, the image's reconstructed spectral axis should provide just a single line with minimal amount of side lobes near it. For an image-quality comparison, all images have been normalized to the maximal value in order to enable better visibility of contrast and resolution improvements.

## 6. Results

In order to evaluate the *EsrSr* and *EsrSrU* algorithms we compared their outputs to those of the *FBP* algorithm. We used as input for the algorithms a set of projections based on a simulated test sample as well as projections acquired in real experiments with well-defined samples.

### 6.1. Simulated test data

#### 6.1.1. Spatial–spatial

**6.1.1.1. Qualitative results.** We begin by looking at the reconstruction results for a Shepp–Logan phantom, which was chosen because it is commonly employed in the literature and it allows for evaluating the quality of the reconstruction algorithm in terms of noise, resolution, and contrast altogether. The noise can be evaluated by observing the smoothness of the background, as the background in the phantom is completely flat. Another method to

evaluate noise is to observe the uniform areas inside the phantom. A good method to evaluate the resolution of the final image is to observe the width of the phantom's contour; the wider the contour, the worse the image resolution. Contrast can be evaluated when comparing the signal intensity in the central hot spot to its uniform background.

Fig. 2 shows an example of typical image reconstruction results for a low SNR Shepp–Logan phantom using a relatively low field modulation amplitude that is equal to the linewidth. Comparing the *FBP* (Fig. 2B) to the result of the *EsrSrU* (Fig. 2D), it is clear that the granular noise inside the phantom's uniform areas and in the background is much more dominant in the *FBP* image. Also, when *EsrSr* starts from the *FBP* image as an initial condition, it clears away some of this kind of noise. Moreover, the phantom's circular contour has a higher intensity in *EsrSr* than in *FBP*, closer to that of the original phantom. The width of the contour accounting for the resolution of the reconstruction is similar in all three cases. Central hot-spot contrast is better in *EsrSrU* as the background has lower intensity and the hot spot has higher intensity than in the *FBP* and *EsrSr*.

Fig. 3 simulates the effects of increasing  $B_m$  from  $\tau$  to  $1.5\tau$ , which increases the SNR from 2 to 3. (When using larger modulation amplitudes, the projection's SNR should improve almost linearly with the modulation amplitude – up to  $B_m = 2\tau$  [59]). When comparing Fig. 3 to Fig. 2 it is clear that the background noise has decreased in all the algorithms, but there is a small resolution deterioration of the contour. It is also apparent that the *EsrSrU* (Fig. 3D) can reconstruct the image better than the *FBP* (Fig. 3B), under these overmodulation conditions. This is because the phan-

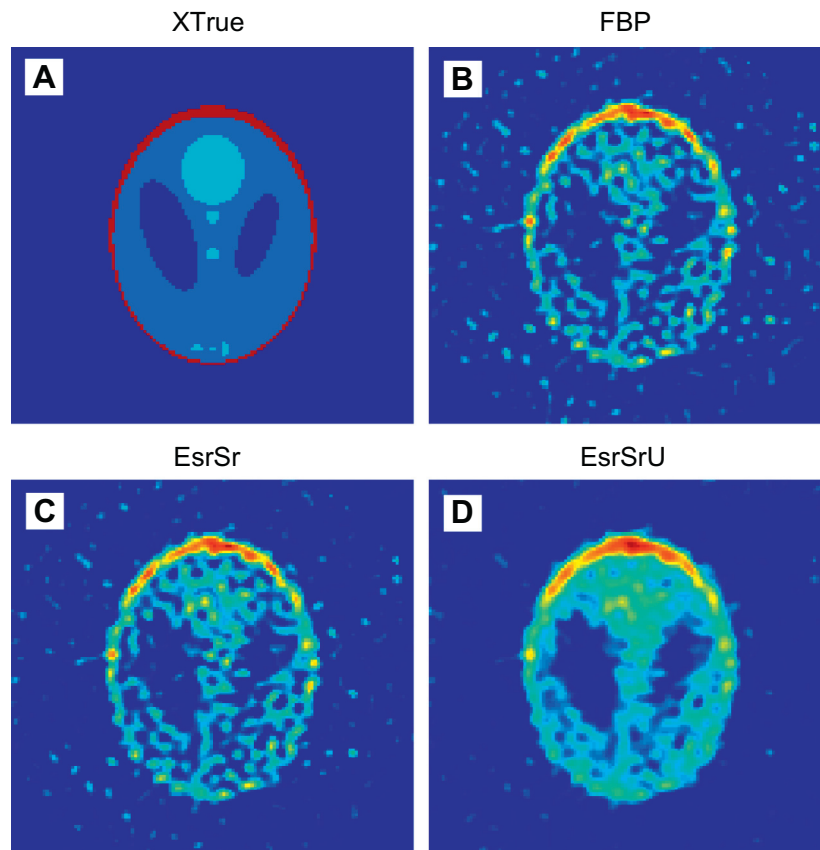


**Fig. 2.** Spatial–spatial phantom reconstruction results: (A) the original image (denoted XTrue); (B) the *FBP* results after negative value cancelation; (C) the *EsrSr* algorithm-reconstructed image using nonnegativity constraints and the *FBP* image as the initial image; (D) same as (C) but using a uniform image as initial image (denoted *EsrSrU*). In all images, the projection SNR = 2 and the modulation amplitude,  $B_m$ , is equal to the FWHM line-width of the given ESR spectrum ( $B_m = \tau$ ).

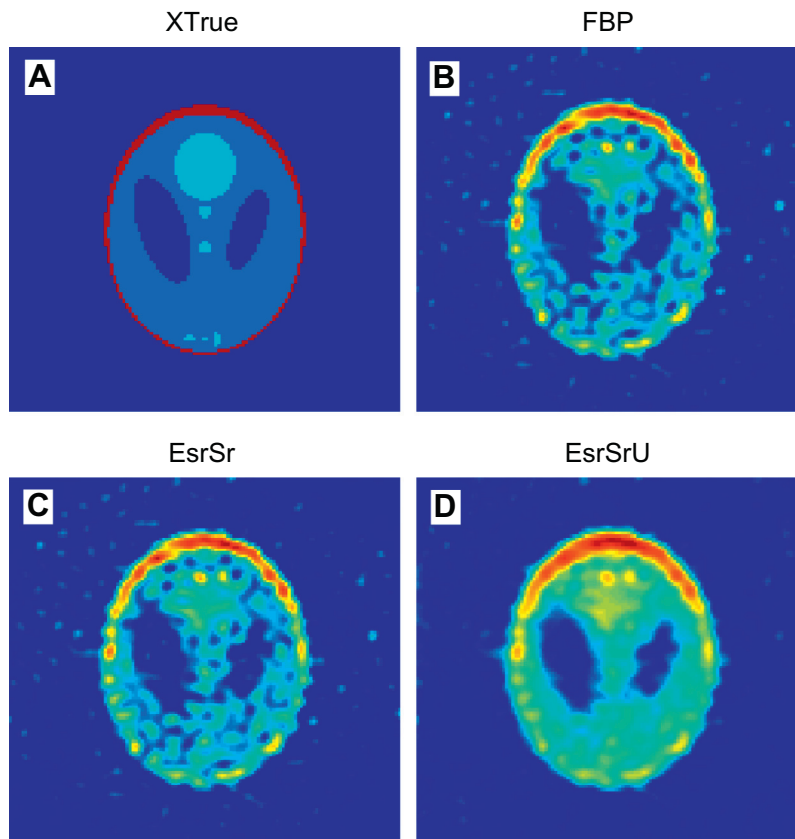


Fig. 3. Same as Fig. 2, but with SNR = 3 and  $B_m = 1.5\tau$ .

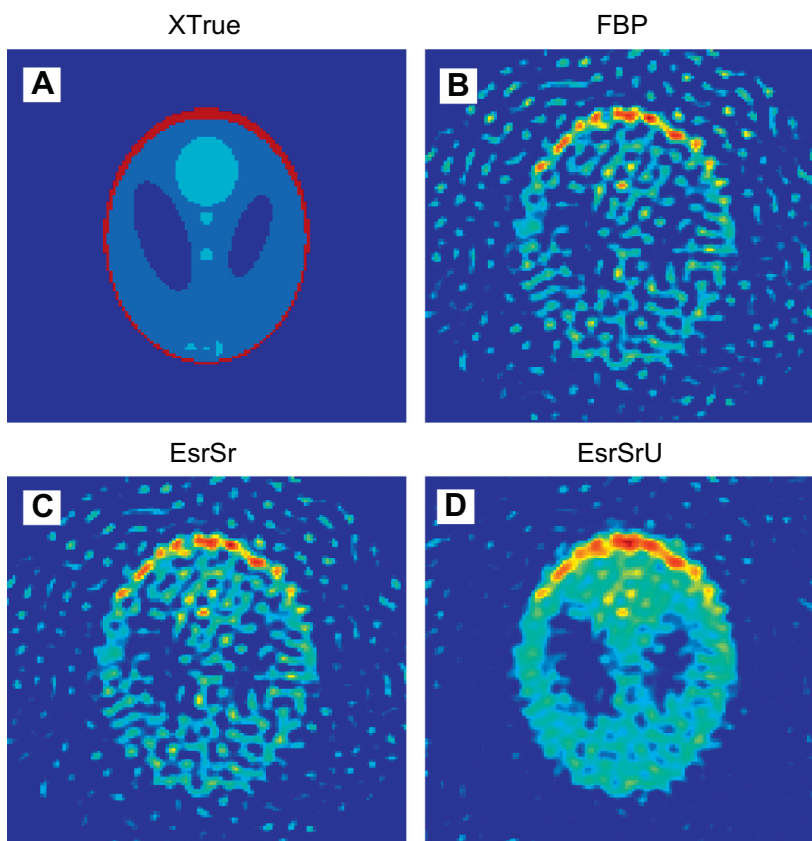


Fig. 4. Same as Fig. 2, but with SNR = 4 and  $B_m = 2\tau$ .

tom’s background and flat areas are smoother. Furthermore, the width of the phantom contour shows that the statistical methods (Fig. 3C and D) recover the resolution as good as FBP (Fig. 3B).

Fig. 4 presents yet another case where modulation amplitude is increased to two times  $\tau$  (with a corresponding increase in projection SNR). This causes a deterioration of the projections’ resolution, and as a result the resolution of the final image is also degraded. This can be seen in all three reconstructed images when comparing Fig. 4 to Fig. 3. Moreover, it is clearly seen that the granularity noise in the uniform areas is accentuated compared to Fig. 2, but noise in the EsrSrU (Fig. 4D) is still considerably lower than in the FBP algorithm (Fig. 4B). However, the SNR increase in the projections fails to improve the overall image quality as the recovery of the over-modulation is not as effective as in Fig. 3.

**6.1.1.2. Quantitative results.** As noted above, our goal is to improve the reconstructed image quality under the constraints of low SNR and/or a relatively small number of projections. In order to evaluate the quality of the reconstructed images for the Shepp–Logan phantom in a quantitative manner, we compared the RSE and MSE vs. SNR for three different modulation amplitudes. This quantitative image analysis is presented in Fig. 5. It should be noted that in this type of analysis, the reconstruction regularization parameters are held constant for each modulation over the entire SNR span, i.e.,  $f_c$  for FBP and  $\beta$  and for the statistical method. On all three graphs it is clear that, for a low SNR of up to  $\sim 2$ , EsrSr and EsrSrU yield a better MSE than FBP, with EsrSrU having an MSE that is about 15% better than EsrSr. For a high SNR of more than 6, it seems that EsrSrU is inferior to FBP and EsrSr, which are both at the same MSE level. When considering the RSE, then EsrSrU is the best in all SNR levels and for all tested modulation amplitudes.

**6.1.2. Spectral-2D spatial imaging**

The Shepp–Logan phantom was generalized to the case of spectral–spatial imaging, as can be seen in Fig. 6A. Three different materials were simulated, with FWHM of 2 G (material 1 – red), 1 G (material 2 – green), and 0.5 G (material 3 – orange). Such kind of phantom can represent, for example, samples that are relevant for oximetry measurements where all of the materials have the same  $g$  value and spectral line-shape but different line-widths. In these simulated results we show the central slice in the spectral dimension and the 1D cut along the spectral dimension. Here we note  $\tau_{min}$  as the intrinsic FWHM of the material with the smallest line-width (material 3). In order to evaluate the contribution of the algorithm under the constraint of a limited number of projections, a relatively low number of only 512 projections were used. Further to that, the projection’s SNR was kept at a medium level of 10–15, which still produces reasonable images. The spectral–spatial theta angle was kept at a rather high  $86.3^\circ$ , so this will not be the factor limiting image quality.

Figs. 6B–D shows the reconstructed images in the case of SNR = 10 and a modulation amplitude equal to  $2\tau_{min}$ . It is clear that the limiting factor in this case is the small number of projections, which leads to streaks artifacts apparent in the FBP image (Fig. 6B), while these artifacts are less significant in the EsrSr and EsrSrU images (Figs. 6C–D). The phantom’s uniform regions are smoother in the EsrSrU (Fig. 6D) than in the other images. The larger central spot of material 1 has better contrast but poorer resolution in EsrSrU (Fig. 6D) compared to the FBP and EsrSr (Figs. 6B and C). The EsrSrU removes the small hot spot underneath the large one, while FBP and EsrSr preserve it. Finally, EsrSr (Fig. 6C) reduces the streaks in the FBP image, especially in the parts of the phantom where no material is present, while preserving the contrast and resolution of the FBP.

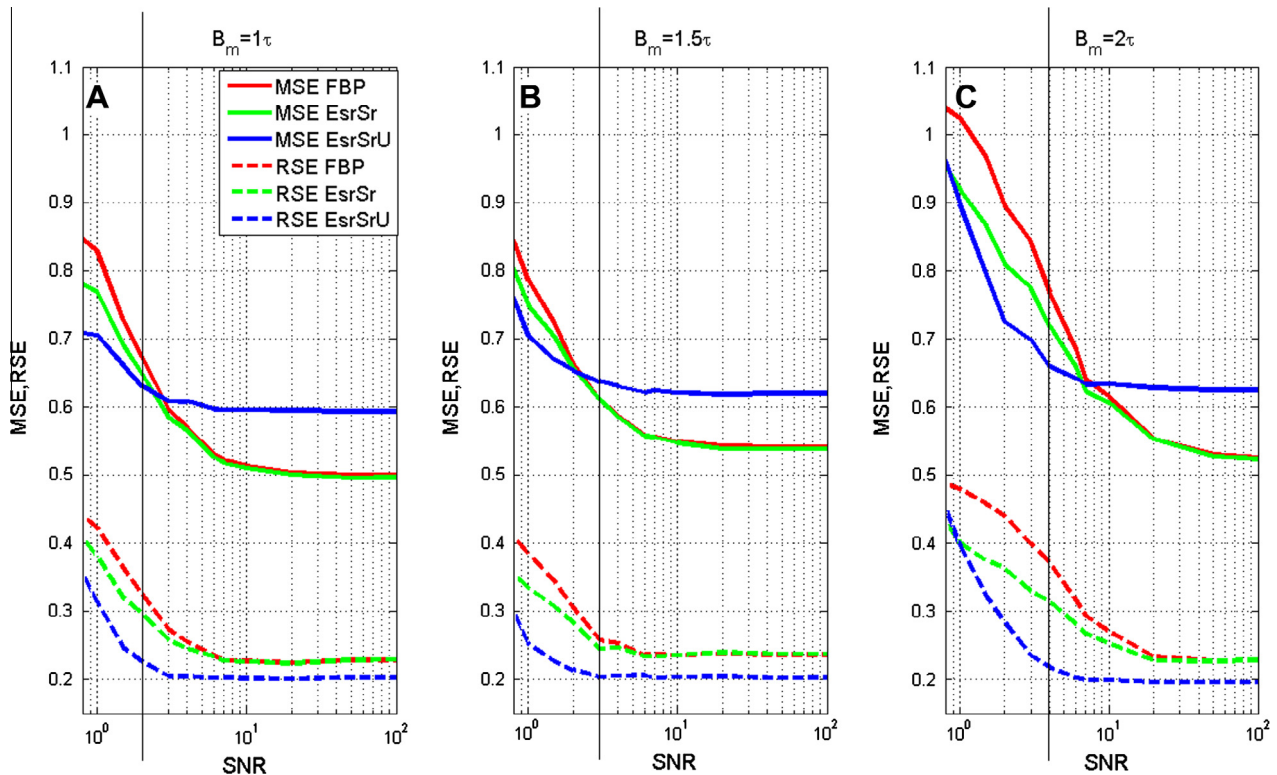


**Fig. 5.** Spatial–spatial – MSE and RSE vs. SNR for different modulation intensities. (A) Modulation amplitude  $B_m$  is equal to  $\tau$ , (B)  $B_m = 1.5\tau$  and (C)  $B_m = 2\tau$ . The SNR is plotted in a logarithmic scale for values from 0.8 to 100 while the number of projections is held constant in this simulation (see Section 5.3.1). The three dotted vertical lines indicate the working points presented in Figs. 2–4, respectively.

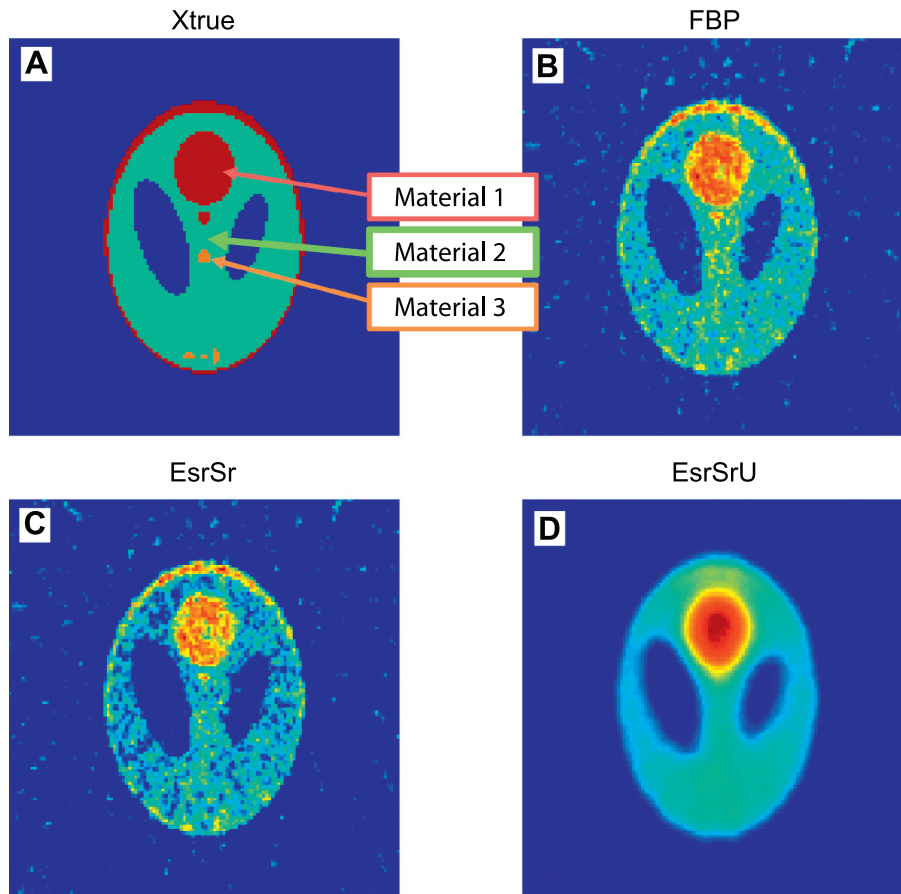


**Fig. 6.** Spectral-2D spatial phantom- central slice image;  $B_m = 2\tau_{\min}$ , SNR = 10. (A) Xtrue – the noiseless phantom; (B) FBP–FBP after negative values cancellation; (C) EsrSr – with postreconstruction cancellation of negative values, the initial image is the FBP; (D) EsrSrU – with postreconstruction cancellation of negative values, the initial image is uniform.

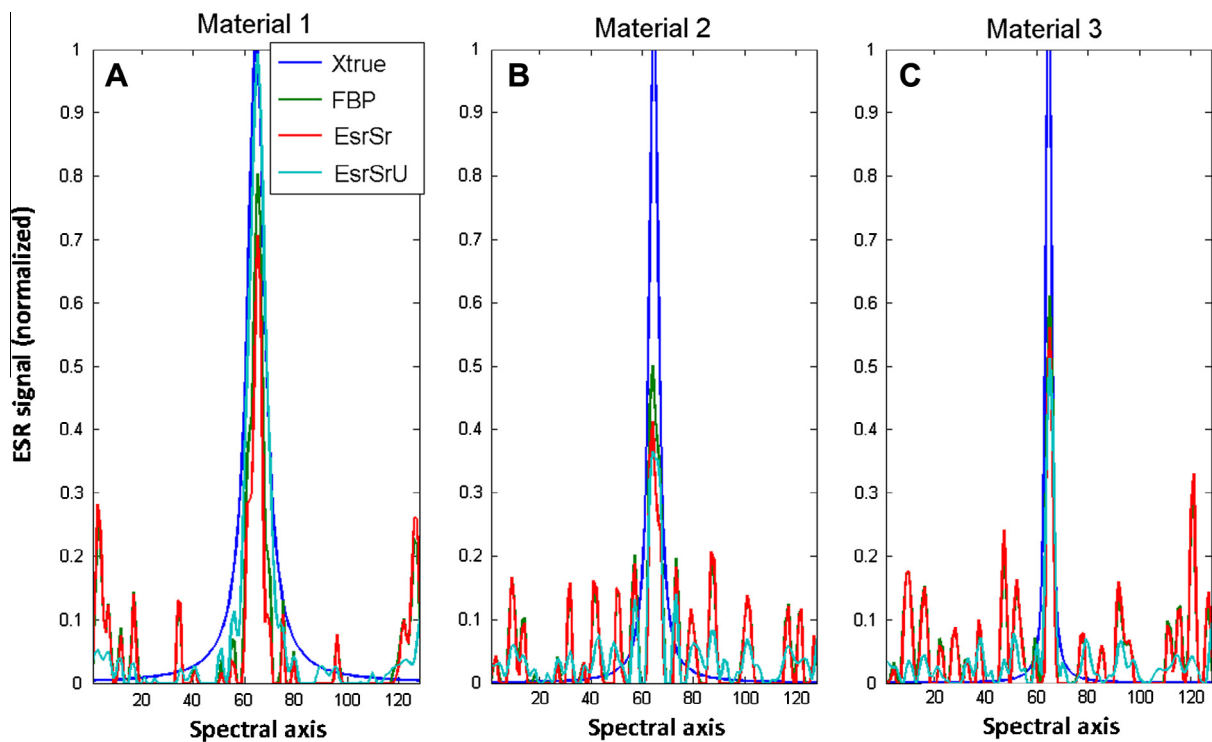


**Fig. 7.** Spectral-2D spatial phantom profiles along the spectral dimension (the 2-Gauss span is divided to 128 points);  $B_m = 2\tau_{\min}$ , SNR = 10. (A) Shows material 1 at the central position in red in Fig. 6 (B) shows material 2 at the central position in green in Fig. 6, finally (C) shows material 3 at the central position in orange in Fig. 6.

**Table 1**  
CRM:CRS for different reconstruction methods.

Case	Reconstruction type	Material 1	Material 2	Material 3
SNR = 10 modulation = $2\tau_{\min}$	FBP	80:23	50:20	60:33
	EsrSr	65:28	42:19	56:26
	EsrSrU	100:9	36:8	52:11
SNR = 15 modulation = $3\tau_{\min}$	FBP	65:16	65:15	56:10
	EsrSr	58:20	60:22	51:15
	EsrSrU	100:7	58:8	56:8

Fig. 7 compares the one-dimensional cut along the spectral axis for the original vs. reconstructed images, for each material at the spatial points indicated in Fig. 6A. The graphs in Fig. 7 show that the spectral line-shape for materials with smaller FWHM is more difficult to recover as it is more strongly affected by the relatively large field modulation amplitude employed in this example. Table 1 summarizes this data in terms of the reconstructed CRM:CRS ratio, which provides an indication of the tradeoff between a large main lobe compared to side-lobe recovery. On the spectral axis of material 1 (Fig. 7A and Table 1), it is clear that EsrSrU fully recovers the spectral peak with very low side lobes, compared to the other methods. As for material 2 (Fig. 7B and Table 1), the CRM of FBP is better than that of the EsrSrU, but the FBP CRS is twice as large as the EsrSrU. In material 3 (Fig. 7C and Table 1), the CRM of FBP is better than that of the EsrSrU by 8%, but the FBP CRS is three times larger than in the EsrSrU method. Also, EsrSr achieves CRM:CRS values that are slightly worse than FBP.

Fig. 8 simulates the effects of going up from  $B_m = 2\tau_{\min}$  to  $B_m = 3\tau_{\min}$ , which increases the SNR from 10 to 15. FBP and EsrSr preserve the small hot spot underneath the large one while in the EsrSrU it is not observed. However, this is at the expense of

small artifactual small hot spots in the central part of the image created by the FBP. The large hot-spot contour in the FBP (Fig. 8B) has a lower contrast compared to the EsrSrU (Fig. 8D). In this case, the EsrSr (Fig. 8C) achieves a poor result as the central hot spot is not uniform, yet streak artifacts of the FBP have been reduced. The comparison between this high modulation amplitude case ( $B_m = 3\tau_{\min}$ , Fig. 8B) and the previous one ( $B_m = 2\tau_{\min}$ , Fig. 6B) shows that the contrast of the central hot spot decreases.

Fig. 9 (and Table 1 that summarizes it) shows the reconstruction results for this case along the image's spectral axis. It is apparent that, for all three materials, the side lobes of the FBP are higher than for the EsrSrU, while the EsrSrU has a main lobe that is comparable in height to that of the FBP. Finally, also in this case EsrSr achieves CRM:CRS values that are slightly worse than FBP. Both Figs. 9 and 7 show the difficulty of recovering the intrinsic line-shape in the presence of a large field modulation. However, in general, the main lobe contrast recovery is better in Fig. 9 compared to Fig. 7 and this is due to the improved SNR.

## 6.2. Experimental data

In addition to the analysis and evaluation carried out with synthetic samples, we also evaluated the performance of our algorithm with real experimental data.

### 6.2.1. Spatial-spatial imaging

A picture of the sample used in our experiments is shown in Fig. 10A. It contains many microcrystals with quite a wide range of sizes that seem to be distributed more or less in a homogenous manner, with occasional clustering. The 2D spatial ESR image of this sample is shown in Fig. 11A. It is apparent that, unlike the opti-

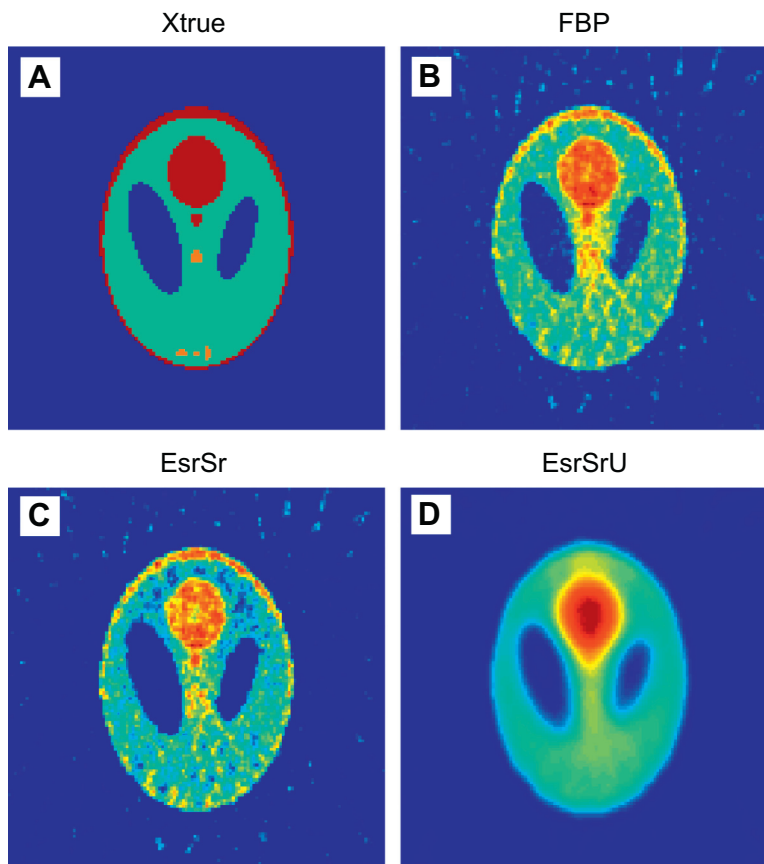


**Fig. 8.** Same as Fig. 6, but with  $B_m = 3\tau_{\min}$  and projection SNR = 15.

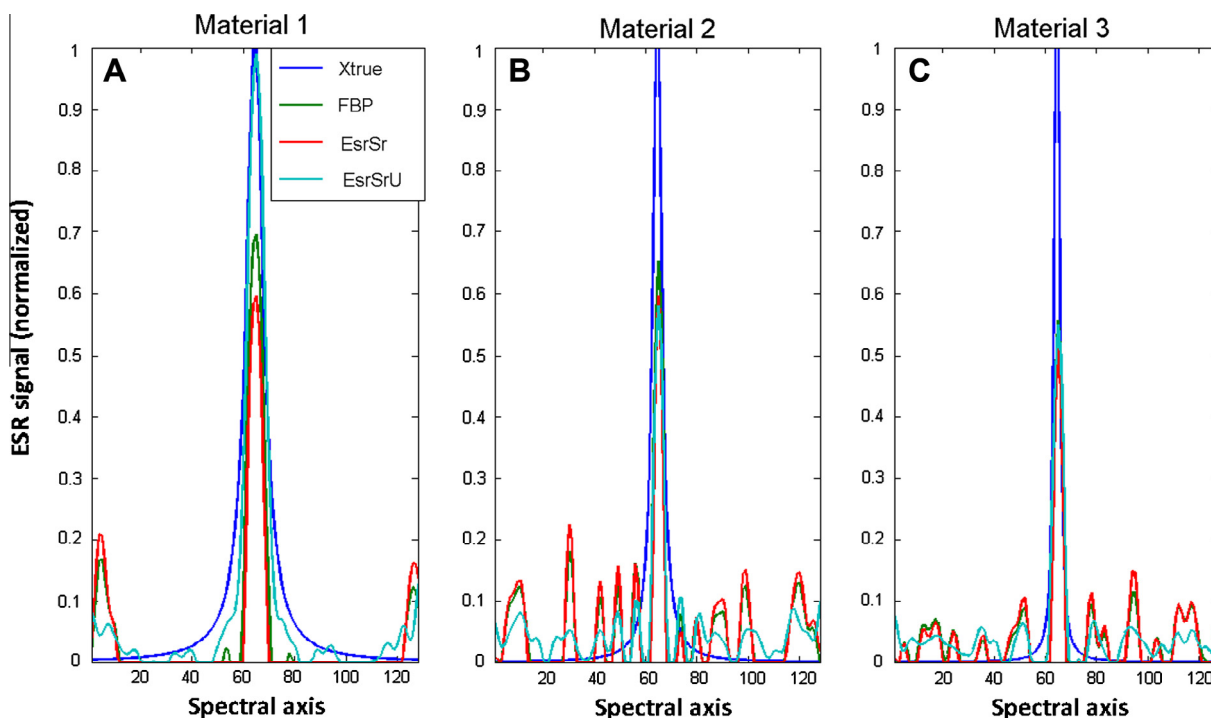


**Fig. 9.** Spectral-2D spatial phantom profiles along the spectral dimension (the 2-Gauss span is divided to 128 points);  $B_m = 3\tau_{\min}$ , SNR = 15. (A) Material 1 at the central position in red in Fig. 6, (B) Material 2 at the central position in green in Fig. 6, finally (C) Material 3 at the central position in orange in Fig. 6.

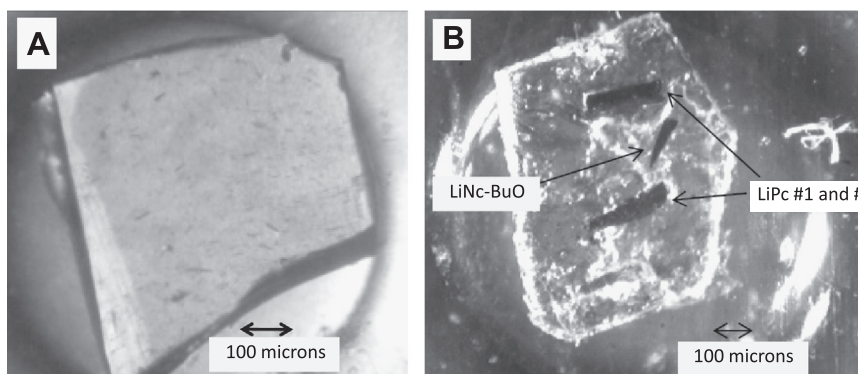


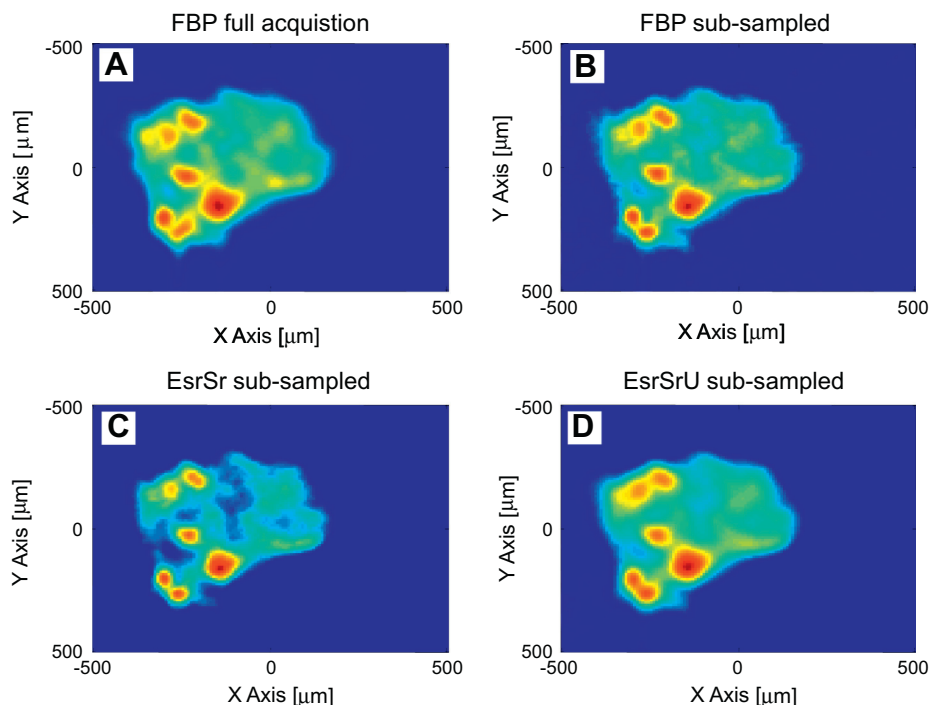
**Fig. 10.** (A) Optical image of the LiNC-BuO sample used in our 2D spatial imaging experiments. (B) Optical image of a sample containing both LiPc and LiNC-BuO crystals employed in our spectral-2D spatial imaging experiments.

cal image, most of the signal originates from  $\sim 6$  to 7 dominant crystals or clusters of crystals. The subsampled FBP image (Fig. 11B) shows streak artifacts that are visible in the left part of the image, and the dominant crystals are blurred compared to a full acquisition (Fig. 11A). The contrast of the hot spots in the EsrSr and EsrSrU images is better than in the subsampled FBP (Fig. 11C) and almost as good as in the original FBP full acquisition (Fig. 11A). When comparing the background of the dominant crystals it is clear that the EsrSrU leads to the smoothest background of all. The resolution can be evaluated by the separation between the two dominant lower-left crystals; in this matter EsrSr makes it possible to clearly separate those two spots better than the other algorithms. This shows how our iterative algorithm is less sensitive to low numbers of projections.

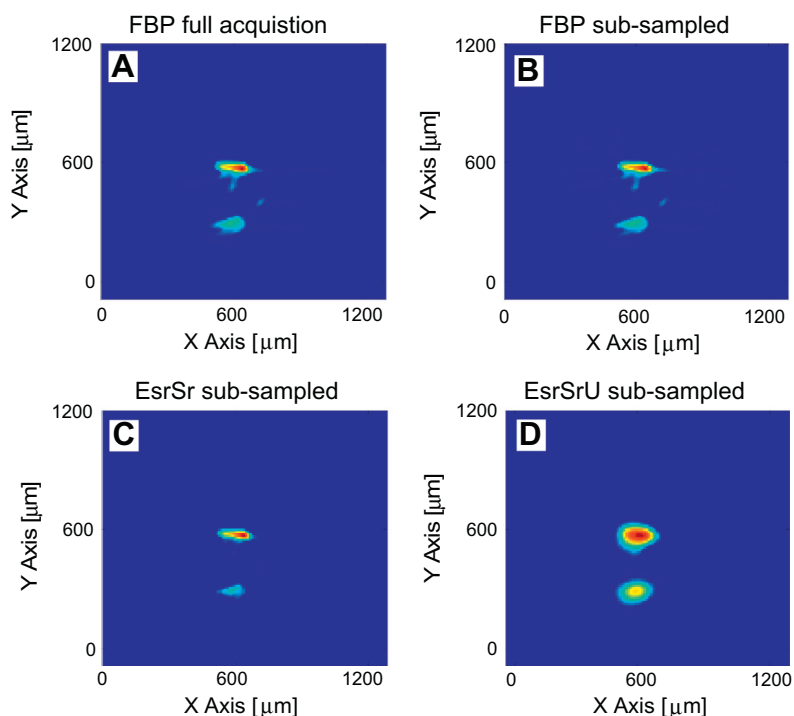
### 6.2.2. Spectral-2D spatial imaging

Fig. 10B shows an optical image of the sample used for the spectral-2D spatial experiments and Figs. 12 and 13 show the 2D reconstructed ESR images at two different spectral positions. The sample

contains one crystal of LiPc and two crystals of LiNC-BuO, prepared under an argon atmosphere, so that their linewidth is less than 1 G. These two different materials are at their maximal spectral intensity at different position in the spectral axis, as shown in Figs. 12A and 13A. The number of projections used in the raw data is 4 times larger than in the subsampled images. The FBP subsampled reconstruction (Figs. 12B and 13B) shows some streak artifacts due to the limited number of projections when comparing it to the full acquisition. These artifacts are almost eliminated completely in the EsrSr and EsrSrU reconstruction results (Figs. 12C and D), leading to an even smoother background than in the full acquisition (Fig. 12A). In the LiNC-BuO slice (Fig. 13), the signal of the LiNC-BuO crystal in EsrSr and EsrSrU (Fig. 13 C and D) is enhanced compared to the signal of the LiPc crystals in the same slice. The contrast and resolution in the images of the three crystals is similar in the FBP subsampled and EsrSr subsampled modes, and is almost as good as in the FBP full acquisition. The EsrSrU presents the best contrast, but on the other hand it provides the worst resolution for all three crystals.



**Fig. 11.** 2D ESR images of the LiNc-BuO sample with  $B_m = \tau$ . While full acquisition refers to 256 projections, subsampled data refers to 64 projections. (A) *FBP*: full acquisition; (B) *FBP*: subsampled; (C) *EsrSr* subsampled: starting from an *FBP* image; (D) *EsrSrU* subsampled: starting at a uniform image.



**Fig. 12.** Spatially-resolved ESR spectra: spatial-spatial slices for LiPc spectrum,  $B_m = \tau_{\min}$ . While full acquisition refers to 4096 projections, subsampled data refers to 1024 projections. (A) *FBP* – full acquisition, (B) *FBP* – subsampled (C) *EsrSr* – subsampled, (D) *EsrSrU* – subsampled.

## 7. Discussion

The results we provide for synthetic samples and the actual experimental data bring with them several key insights.

### 7.1. Spatial-spatial images

The image quality for the experimental (Fig. 11) and simulation (Figs. 2–4) results clearly shows that the *EsrSr* slightly improves

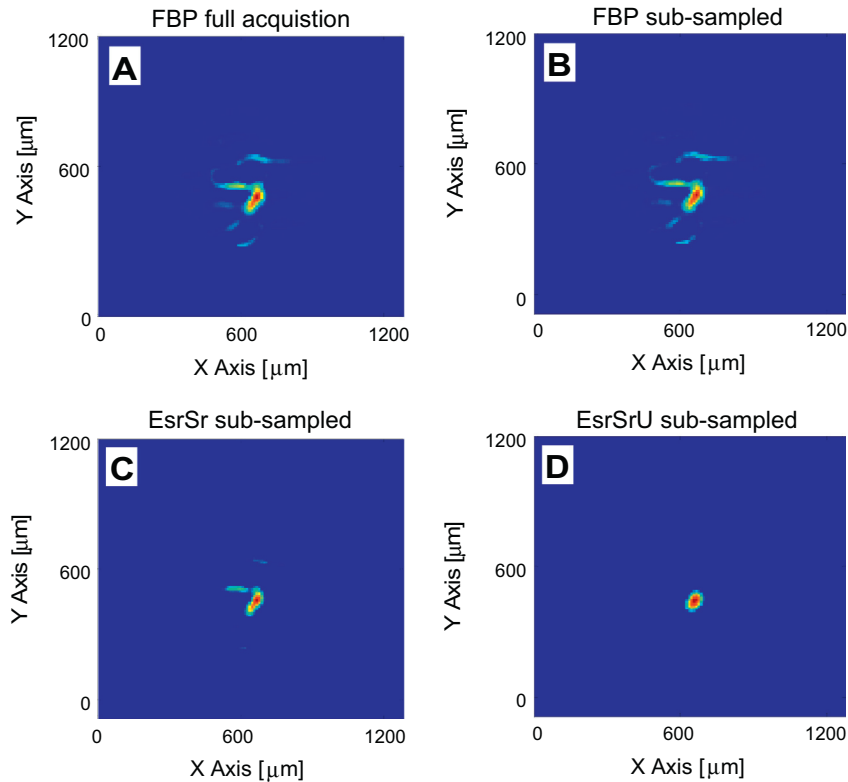


**Fig. 13.** As in Fig. 12, spatial-spatial slices for LiNc-BuO spectrum, (A) *FBP* Full acquisition, (B) *FBP* – subsampled, (C) *EsrSr* – subsampled, and finally (D) *EsrSrU* – subsampled.

the image SNR (by removing some of the streak artifacts and the granular noise) compared to the *FBP* while maintaining resolution and contrast. On the other hand, the *EsrSrU* shows improved contrast and SNR but also a somewhat degraded resolution. This is because convergence rates and optimal solution depend on the starting conditions of the algorithms, and when starting with the *FBP* image high frequencies emerge relatively fast. Such observation is true also for the spectral-spatial images. As for the modulation amplitude, from our analysis it is seen that a field modulation of up to  $1.5\tau$  (Fig. 3) is beneficial and improves the images both qualitatively and quantitatively. In the range of  $2\tau$  (Fig. 4), the quantitative image parameters (Fig. 5) of *EsrSr* are improved compared to a smaller modulation, but the visual effect of granularity noise is unattractive in practice. When comparing a modulation amplitude of  $1\tau$  (Fig. 2) to higher modulation amplitudes, it is clear that the edges are wider and resolution is lower, but up to  $1.5\tau$  this smoothing is acceptable in our test set. The contrast of the hot spot also improves when moving from  $1\tau$  to  $1.5\tau$ , but decreases again when using a modulation amplitude of  $2\tau$ . Thus, it seems that a modulation of  $1.5\tau$  is a good compromise for a better SNR while keeping a fair contrast and resolution.

### 7.2. Spectral-spatial images

Our present approach to spectral-spatial image reconstruction avoids the pre-integration of the projections and uses the statistical framework to overcome the “limited angle” problem and the issue of de-noising by regularization. The method is nonparametric as compared to other advanced reconstruction algorithms that employ a parametric approach (such as [60]). Nevertheless, after reconstruction, it is possible to acquire the FWHM of the original line-shape using curve fitting as described in [18,19].

The influence of field-modulation magnitude on spectral-spatial image quality can be obtained from Figs. 6 and 8. It is seen

that overmodulation affects mildly the image quality of the *FBP* central slice, mainly reducing the contrast of hot spots compared to the background. Such effects are corrected by the *EsrSr* method. The *EsrSrU* central slice keeps a uniform background and better central hot spot contrast when higher modulation is used. Large field modulations in the range of  $3\tau_{\min}$  may be beneficial in some cases where the spectral profile shows lower side lobes when compared to  $2\tau_{\min}$ , which is good if the goal is to obtain a less noisy out-of-peak spectral signal. Moreover, main-lobe contrast recovery is much better when using an over-modulation of  $3\tau_{\min}$  and this can help to calculate the FWHM of the main peak more easily.

### 7.3. *FBP* cutoff frequency $f_c$ vs. statistical reconstruction penalty $\beta$

In conventional *FBP* image reconstruction, the tradeoff between noise and resolution is controlled by adjusting the cutoff frequency,  $f_c$ , of the back-projection filter. Since  $f_c$  has units of inverse length [61], there is an intuitive and object-independent relationship between  $f_c$  and the resolution of the reconstructed images. In the iterative statistical reconstruction method the regularization parameter,  $\beta$ , plays a role similar to that of the  $f_c$ . A possible disadvantage of using regularization terms in the statistical method may be the absence of an intuitive method for choosing the value of the regularization parameter,  $\beta$ , even for simple quadratic penalties. However, the results in Fig. 5 demonstrate that a constant  $\beta$  fits a large range of SNRs. In all our 2D-spatial and spectral-2D spatial simulations,  $\beta$  and  $f_c$  were held constant for all SNR values and modulations. In low SNRs, better qualitative results and measurements were achieved using the statistical methods rather than *FBP*. This demonstrates that our penalty function is impervious to major changes in the input’s noise and modulation.

#### 7.4. Edge preservation – regularization function

In Figs. 2–4, 6 and 8 the contour of the *EsrSrU* is smoother than in the *FBP*. It is well known that quadratic regularization tends to oversmooth sharp edges [62]. Our model assumes that samples taken from a physical object are unlikely to be piecewise constant in the spatial dimensions, and that  $w_c$  controls the roughness of the spectral dimension. This assumption does not hold in the case to the Shepp–Logan’s contour, as it is similar to a radial apodization function. In piecewise constant phantoms, some nonconvex regularization functions have shown good results [63]. However, Bournan and Sauer [54] have shown that nonconvex penalties lead to estimates that are *discontinuous functions of measurements*. This means that a slight change in the measurements could significantly change the reconstructed image. In cases where the object under study is indeed piecewise constant, there is no doubt that nonquadratic penalties give a better noise/resolution tradeoff [64]. Nevertheless, in the experimental field of ESRI, most samples fit into our model of mild variation of the intensity.

#### 7.5. Comparing *EsrSrU* and *EsrSr* image quality

The need to build high frequencies from uniform images results in slow convergence of *EsrSrU* imaging, whereas *EsrSr* imaging that starts from an *FBP* image containing high frequencies converges faster. As we use a local optimization algorithm, cases that start with an *FBP* image which may contain artifacts result in *EsrSr* that is constrained to converge toward an image that still suffers from those artifacts (e.g., Fig. 8C). Conversely, *EsrSrU* de-noising of granular and streak noises is very effective (Figs. 3D and 8D). In terms of MSE and RSE in low SNRs, *FBP* and *EsrSr* images are suboptimal compared to the *EsrSrU* final image for all modulation amplitudes tested. When *FBP* images contain fewer artifacts, as in the experimental data given in this manuscript, *EsrSr* yields less background noise while retaining *FBP* resolution and contrast. In those cases, *EsrSrU* produces images that are smoother than *EsrSr* images and have a lower contrast. Finally, *EsrSr* can serve as a good compromise when run time is a consideration, especially in high-dimensional processing. Alternatively, *EsrSrU* is a viable solution to the problem of a low SNR and small number of projections.

#### 7.6. Computational cost

The most computationally-intensive part of any iterative reconstruction algorithm is forward and backward projections. While in the *FBP* there is only one back-projection, in every iteration of the statistical method there is one forward and one backward projection, which is twice more intensive. As mentioned above, *EsrSrU* has a longer convergence time than *EsrSr*. A good rule of thumb is that *EsrSrU* requires twice more iterations for convergence than *EsrSr*. In the case of 2D-spatial and spectral-2D spatial imaging, *EsrSrU* requires about 10 and 30 iterations respectively in order to converge on our test set. This means that the *EsrSrU* algorithm is 20 to 60 times more computationally intensive than *FBP*, while *EsrSr* is half as intensive. When the computation platform described in Section 5.1 is used for simulation reconstruction, *EsrSrU* runs for about 20 s in the 2D-spatial case (reconstructed image size:  $128^2$  pixels) and it runs for about 15 min in the spectral-2D spatial case (reconstructed image size:  $128^3$  voxels).

#### 7.7. Limitations of our model

There are several limitations to our model worth mentioning. To begin with, we do not take into account distortions additional to white Gaussian noises, such as the instability of baselines and of resonator frequency. Shifts in resonator frequency cause shifts

in the ESR spectra and may be accompanied by phase shifts that cause dispersion signals and mixtures. Small frequency shifts cause the broadening of peaks in the reconstructed image, while larger shifts could result in spurious peaks. The discrepancy between experimental projections and ideal projections caused by a frequency shift is signal-dependent. While it may be larger than white Gaussian noise in regions with high signal intensities, it may vanish in regions with intensities close to the baseline. Finally, in the case of spectral-2D spatial imaging, we use the average line-width for the deconvolution process (see Section 3.2.3). This approximation of the physical effect holds up to two times the average line-width in our experiments (smaller or larger than the average). For larger line-width differences, the deconvolution process may deform the reconstructed line-shape.

#### Acknowledgments

I.K. would like to thank the Technion’s Signal & Image Processing Lab for their generous technical support; without their powerful servers, work on this paper would have been delayed considerably. This work was partially supported by Grant #201665 from the European Research Council (ERC).

#### References

- [1] G.R. Eaton, S.S. Eaton, K. Ohno, *EPR Imaging and In Vivo EPR*, CRC Press, Boca Raton, 1991.
- [2] S.K. Misra (Ed.), *Multifrequency ELECTRON Paramagnetic Resonance, Theory and Applications*, Wiley-VCH, Berlin, 2011.
- [3] M. Ikeya, *Electron-Spin-Resonance (ESR) microscopy in materials science*, *Annu. Rev. Mater. Sci.* 21 (1991) 45–63.
- [4] G. Ilangovan, T. Liebgott, V.K. Kutala, S. Petryakov, J.L. Zweier, P. Kuppusamy, *EPR oximetry in the beating heart: myocardial oxygen consumption rate as an index of postschismic recovery*, *Magn. Reson. Med.* 51 (2004) 835–842.
- [5] D.J. Lurie, K. Mader, *Monitoring drug delivery processes by EPR and related techniques – principles and applications*, *Adv. Drug. Deliver. Rev.* 57 (2005) 1171–1190.
- [6] A. Blank, J.H. Freed, N.P. Kumar, C.H. Wang, *Electron spin resonance microscopy applied to the study of controlled drug release*, *J. Controlled Release* 111 (2006) 174–184.
- [7] T.J. Reddy, T. Iwama, H.J. Halpern, V.H. Rawal, *General synthesis of persistent trityl radicals for EPR imaging of biological systems*, *J. Org. Chem.* 67 (2002) 4635–4639.
- [8] R.P. Pandian, N.L. Parinandi, G. Ilangovan, J.L. Zweier, P. Kuppusamy, *Novel particulate spin probe for targeted determination of oxygen in cells and tissues*, *Free Radic. Biol. Med.* 35 (2003) 1138–1148.
- [9] J. Radon, *On the determination of functions from their integral values along certain manifolds*, *IEEE Trans. Med. Imaging* 5 (1986) 170–176.
- [10] L.A. Shepp, B.F. Logan, *The Fourier reconstruction of a head section*, *IEEE Trans. Nucl. Sci.* 21 (1974) 21–43.
- [11] G.N. Ramachandran, A.V. Lakshminarayanan, *3-Dimensional reconstruction from radiographs and electron micrographs – application of convolutions instead of Fourier transforms*, *Proc. Natl. Acad. Sci. U.S.A.* 68 (1971) 2236.
- [12] T. Chang, G.T. Herman, *A scientific study of filter selection for a fan-beam convolution reconstruction algorithm*, *SIAM J. Appl. Math.* 39 (1980) 83–105.
- [13] F. Momo, S. Colacicchi, A. Sotgiu, *Limits of deconvolution in enhancing the resolution in EPR imaging experiments*, *Meas. Sci. Technol.* 4 (1993) 60–64.
- [14] M.M. Maltempo, S.S. Eaton, G.R. Eaton, *Spectral-spatial two-dimensional electron-paramagnetic-res imaging*, *J. Magn. Reson.* 72 (1987) 449–455.
- [15] M.M. Maltempo, S.S. Eaton, G.R. Eaton, *Reconstruction of spectral-spatial two-dimensional EPR images from incomplete sets of projections without prior knowledge of the component spectra*, *J. Magn. Reson.* 77 (1988) (1969) 75–83.
- [16] J.H. Kim, K.Y. Kwak, S.B. Park, Z.H. Cho, *Projection space iteration reconstruction reprojection*, *IEEE Trans. Med. Imaging* 4 (1985) 139–143.
- [17] K.H. Ahn, H.J. Halpern, *Comparison of local and global angular interpolation applied to spectral-spatial EPR image reconstruction*, *Med. Phys.* 34 (2007) 1047–1052.
- [18] Y.M. Deng, R.P. Pandian, R. Ahmad, P. Kuppusamy, J.L. Zweier, *Application of magnetic field over-modulation for improved EPR linewidth measurements using probes with Lorentzian lineshape*, *J. Magn. Reson.* 181 (2006) 254–261.
- [19] C. Mailer, B.H. Robinson, B.B. Williams, H.J. Halpern, *Spectral fitting: the extraction of crucial information from a spectrum and a spectral image*, *Magn. Reson. Med.* 49 (2003) 1175–1180.
- [20] C.R. Crawford, A.C. Kak, *Aliasing artifacts in computerized tomography*, *Appl. Opt.* 18 (1979) 3704–3711.
- [21] C.M. Smith, A.D. Stevens, *Reconstruction of images from radiofrequency electron-paramagnetic-resonance spectra*, *Br. J. Radiol.* 67 (1994) 1186–1195.

- [22] A.I. Smirnov, Post-processing of EPR spectra by convolution filtering: calculation of a harmonics' series and automatic separation of fast-motion components from spin-label EPR spectra, *J. Magn. Reson.* 190 (2008) 154–159.
- [23] R. Gordon, R. Bender, G.T. Herman, Algebraic Reconstruction Techniques (ART) for 3-dimensional electron microscopy and X-ray photography, *J. Theor. Biol.* 29 (1970) 471.
- [24] S. Sivakumar, M.C. Krishna, R. Murugesan, Evaluation of algebraic iterative algorithms for reconstruction of electron magnetic resonance images, in: Fourth Indian Conference on Computer Vision, Graphics & Image Processing, 2004, pp. 353–358.
- [25] J.A. Fessler, Iterative image reconstruction for CT, AAPM Image Educational Course – Image Reconstruction II, 2011.
- [26] E. Veklerov, J. Llacer, Stopping rule for the MLE algorithm based on statistical hypothesis-testing, *IEEE Trans. Med. Imaging* 6 (1987) 313–319.
- [27] D.L. Snyder, M.I. Miller, L.J. Thomas, D.G. Polite, Noise and edge artifacts in maximum-likelihood reconstructions for emission tomography, *IEEE Trans. Med. Imaging* 6 (1987) 228–238.
- [28] K. Lange, Convergence of EM image-reconstruction algorithms with Gibbs smoothing, *IEEE Trans. Med. Imaging* 9 (1990) 439–446.
- [29] R. Leahy, X. Yan, Statistical models and methods for PET image reconstruction, *Ann. Meeting Am. Stat. Assoc.* (1991) 1–10.
- [30] J.A. Fessler, N.H. Clinthorne, W.L. Rogers, Regularized emission image-reconstruction using imperfect side information, *IEEE Trans. Nucl. Sci.* 39 (1992) 1464–1471.
- [31] J.A. Fessler, W.L. Rogers, Spatial resolution properties of penalized-likelihood image reconstruction: space-invariant tomographs, *IEEE Trans. Image Process.* 5 (1996) 1346–1358.
- [32] J. Skilling, R.K. Bryan, Maximum-entropy image-reconstruction – general algorithm, *Mon. Not. R. Astron. Soc.* 211 (1984) 111.
- [33] C.A. Johnson, D. McGarry, J.A. Cook, N. Devasahayam, J.B. Mitchell, S. Subramanian, M.C. Krishna, Maximum entropy reconstruction methods in electron paramagnetic resonance imaging, *Ann. Oper. Res.* 119 (2003) 101–118.
- [34] M. Tseitlin, A. Dhami, S.S. Eaton, G.R. Eaton, Comparison of maximum entropy and filtered back-projection methods to reconstruct rapid-scan EPR images, *J. Magn. Reson.* 184 (2007) 157–168.
- [35] P.E. Kinahan, J.A. Fessler, J.S. Karp, Statistical image reconstruction in PET with compensation for missing data, *IEEE Trans. Nucl. Sci.* 44 (1997) 1552–1557.
- [36] H. Wahlquist, Modulation broadening of unsaturated Lorentzian lines, *J. Chem. Phys.* 35 (1961) 1708–1710.
- [37] J.S. Hyde, M. Pasenkiewicz-Gierula, A. Lesmanowicz, W.E. Antholine, Pseudo field modulation in EPR spectroscopy, *Appl. Magn. Reson.* 1 (1990) 483–496.
- [38] J.S. Hyde, A. Jesmanowicz, J.J. Ratke, W.E. Antholine, Pseudomodulation – a computer-based strategy for resolution enhancement, *J. Magn. Reson.* 96 (1992) 1–13.
- [39] R.D. Nielsen, E.J. Hustedt, A.H. Beth, B.H. Robinson, Formulation of Zeeman modulation as a signal filter, *J. Magn. Reson.* 170 (2004) 345–371.
- [40] B.H. Robinson, C. Mailer, A.W. Reese, Linewidth analysis of spin labels in liquids – I. Theory and data analysis, *J. Magn. Reson.* 138 (1999) 199–209.
- [41] B.H. Robinson, C. Mailer, A.W. Reese, Linewidth analysis of spin labels in liquids – II, Exp. *J. Magn. Reson.* 138 (1999) 210–219.
- [42] J. Fessler, Image Reconstruction Toolbox, University of Michigan, 2011. <<http://www.eecs.umich.edu/~fessler/code/>>.
- [43] E.W. Weisstein, Radon Transform, from MathWorld—A Wolfram Web Resource.
- [44] J.A. Fessler, Users guide for ASPIRE 3D image reconstruction software, in: Comm. and Sign. Proc. Lab., Dept. of EECS, Univ. of Michigan, Ann Arbor, MI, Tech. Rep. 310, 1997.
- [45] R. Ahmad, D.S. Vikram, L.C. Potter, P. Kuppusamy, Estimation of mean and median  $pO_2$  values for a composite EPR spectrum, *J. Magn. Reson.* 192 (2008) 269–274.
- [46] O.V. Michailovich, A. Tannenbaum, Despeckling of medical ultrasound images, *IEEE Trans. Ultrason. Ferr.* 53 (2006) 64–78.
- [47] K. Lange, R. Carson, EM reconstruction algorithms for emission and transmission tomography, *J. Comput. Assist. Tomogr.* 8 (1984) 306–316.
- [48] M. Yavuz, J.A. Fessler, Statistical image reconstruction methods for randoms-precorrected PET scans, *Med. Image Anal.* 2 (1998) 369–378.
- [49] D.L. Snyder, C.W. Helstrom, A.D. Lanterman, M. Faisal, R.L. White, Compensation for readout noise in CCD images, *J. Opt. Soc. Am. a—Opt. Image Sci. Vision* 12 (1995) 272–283.
- [50] I.A. Elbakri, J.A. Fessler, Efficient and accurate likelihood for iterative image reconstruction in X-ray computed tomography, *Med. Imaging 2003: Image Process.* 5032 (2003) 1839–1850.
- [51] J.A. Fessler, S.D. Booth, Conjugate-gradient preconditioning methods for shift-variant PET image reconstruction, *IEEE Trans. Image Process.* 8 (1999) 688–699.
- [52] P. Tan, C. Drossos, Invariance properties of maximum likelihood estimators, *Math. Magaz.* 48 (1975) 37–41.
- [53] J.A. Fessler, Penalized weighted least-squares image-reconstruction for positron emission tomography, *IEEE Trans. Med. Imaging* 13 (1994) 290–300.
- [54] C. Bournan, K. Sauer, A generalized Gaussian image model for edge-preserving MAP estimation, *IEEE Trans. Image Process.* 2 (1993) 296–310.
- [55] J.A. Fessler, H. Erdogan, A paraboloidal surrogates algorithm for convergent penalized-likelihood emission image reconstruction, *IEEE Conf. Record Nucl. Sci. Symp.* 2 (1998) 1132–1135.
- [56] A.K. Jain, Fundamentals of Digital Image Processing, Prentice Hall, Englewood Cliffs, NJ, 1989, p. 439.
- [57] A. Blank, R. Halevy, M. Shklyar, L. Shtirberg, P. Kuppusamy, ESR micro-imaging of LiNc–BuO crystals in PDMS: spatial and spectral grain distribution, *J. Magn. Reson.* 203 (2010) 150–155.
- [58] Y.K. Dewaraja, K.F. Koral, J.A. Fessler, Regularized reconstruction in quantitative SPECT using CT side information from hybrid imaging, *Phys. Med. Biol.* 55 (2010) 2523–2539.
- [59] C.P. Poole, Electron Spin Resonance: A Comprehensive Treatise on Experimental Techniques, Wiley, New York, 1983 (chapter 6).
- [60] S. Som, L.C. Potter, R. Ahmad, P. Kuppusamy, A parametric approach to spectral-spatial EPR imaging, *J. Magn. Reson.* 186 (2007) 1–10.
- [61] G.T. Gullberg, T.F. Budinger, The use of filtering methods to compensate for constant attenuation in single-photon emission computed-tomography, *IEEE Trans. Biomed. Eng.* 28 (1981) 142–157.
- [62] S. Ahn, R.M. Leahy, Analysis of resolution and noise properties of nonquadratically regularized image reconstruction methods for PET, *IEEE Trans. Med. Imaging* 27 (2008) 413–424.
- [63] R. Chartrand, Nonconvex regularization for shape preservation, in: IEEE International Conference on Image Processing (ICIP), 2007.
- [64] A.L. Lee, A.J. Wand, Assessing potential bias in the determination of rotational correlation times of proteins by NMR relaxation, *J. Biomol. NMR* 13 (1999) 101–112.